metals

MDPI

Review

The Role of Precipitates in Hydrogen Embrittlement of Precipitation-Hardenable Aluminum Alloys

Terezie Košová Altnerová [1,2,*], Darja Rudomilova [1,*], Pavel Novák [2] and Tomáš Prošek [1]

[1] Department of Metallic Materials, University of Chemistry and Technology Prague, Technopark Kralupy, Nám. G. Karse 7, 278 01 Kralupy nad Vltavou, Czech Republic; prosekt@vscht.cz
[2] Department of Metallic Materials and Corrosion Engineering, University of Chemistry and Technology Prague, Technická 5, 166 28 Prague, Czech Republic; panovak@vscht.cz
* Correspondence: altnerot@vscht.cz (T.K.A.); darja.rudomilova@vscht.cz (D.R.); Tel.: +420-220-44-6125 (T.K.A. & D.R.)

Abstract: This review examines hydrogen embrittlement (HE) in precipitation-hardenable aluminum alloys, focusing on the role of precipitates as hydrogen traps. It covers hydrogen entry mechanisms, the effects of microstructural features such as dislocations and grain boundaries, and secondary phase evolution during heat treatment. The interaction between hydrogen and precipitates, including the role of coherent and incoherent interfaces, is analyzed in view of the impact on HE susceptibility. Various techniques used to assess the interaction between hydrogen and aluminum alloys are also compared. The goal is to summarize the state-of-the-art understanding of the microstructural factors influencing the resistance of aluminum alloys to HE.

Keywords: hydrogen embrittlement; aluminum alloys; second phase particles; hydrogen trapping

check for updates

Citation: Košová Altnerová, T.; Rudomilova, D.; Novák, P.; Prošek, T. The Role of Precipitates in Hydrogen Embrittlement of Precipitation-Hardenable Aluminum Alloys. *Metals* **2024**, *14*, 1287. https://doi.org/10.3390/met14111287

Academic Editor: Jin-Yoo Suh

Received: 4 October 2024
Revised: 2 November 2024
Accepted: 5 November 2024
Published: 14 November 2024

1. Introduction

Aluminum stands as the most abundant non-ferrous structural metal, with 8% of the Earth's crust containing aluminum in the form of bauxite, making it an accessible material [1]. Despite its high standard equilibrium potential value, which suggests susceptibility to corrosion, aluminum is successfully used in environments where an oxide layer forms on its surface, serving as a protective barrier. One of the greatest advantages of aluminum is its low density, which enables lightweight constructions; however, its softness poses limitations. Adding specific alloying elements enhances strength while preserving the low density of the final alloy, allowing these materials to be used in very demanding industries such as aerospace or automotive [2].

Precipitation-hardenable aluminum alloys vary in their alloying element composition but share the characteristic that their strengthening is driven by the formation of precipitates [3]. During the aging process, secondary phase particles form, impeding the movement of dislocations and consequently strengthening the material [4–6].

Hydrogen embrittlement (HE) is a complex phenomenon in materials science and engineering, leading to degradation of the mechanical properties of high-strength aluminum alloys [7]. Numerous factors affect susceptibility to HE, including material strength, environment composition, pressure, temperature, exposure duration, strain rate, surface condition, amount of absorbed hydrogen, amount and type of hydrogen trapping sites, and coatings [8]. Precipitates serve as significant hydrogen traps, impacting susceptibility to HE [9]. Moreover, the role of specific elements, microstructural intricacies, and nuances of heat treatment cannot be overlooked.

Several useful reviews on this subject have been published. In 2012, Scully et al. [10] described in detail the interaction between gaseous hydrogen and water environments and selected aluminum alloys, including surface reactions, characterization of trapping sites, hydrogen transport, and HE mechanisms. The review of Lynch et al. [11] is not

specifically focused on the use of aluminum alloys but provides a wealth of information on the mechanisms of HE, linking together hypotheses and existing studies on the subject. Chen et al. [12] focused on HE in aluminum alloys used for hydrogen storage tanks, providing an overview of essential information on the mechanism, detection methods, and prevention of HE.

The purpose of this review is to summarize information on the effect of precipitates in aluminum alloys on HE. The initial section provides an overview of the fundamental mechanisms underlying hydrogen entry and structure–hydrogen interaction, as well as the mechanisms of HE. Additionally, the methods for the detection and evaluation of HE in aluminum and its alloys are described. The second part of this review is devoted to the description of selected series of aluminum alloys, namely 2xxx, 6xxx, 7xxx, and Al–Li. The interaction of hydrogen with secondary phase particles is described in detail, as are the effects of hydrogen on the mechanical properties of the materials at different stages of aging.

2. Principal Factors Controlling Susceptibility to HE

2.1. Hydrogen Entry

HE only occurs when hydrogen is present in the material as a consequence of an interaction with the environment [8]. Based on the source of hydrogen, HE is sometimes divided into two categories: Internal Hydrogen Embrittlement (IHE) and External Hydrogen Embrittlement (EHE). Although this distinction is widely used, it has no fundamental background and can thus be misleading. In IHE, hydrogen is introduced to a material during manufacturing, becoming dissolved in the matrix prior to loading. EHE occurs when a material degrades due to hydrogen from the gaseous environment or as a result of an electrochemical reaction introducing hydrogen during the product's lifetime [13].

2.1.1. Hydrogen Uptake During the Manufacturing Process

The initial critical phase occurs during the production of aluminum itself. Aluminum is typically manufactured through the Hall–Héroult process, which involves reducing alumina in electrolytic cells with a molten cryolite bath [14]. During this process, the electrolyte reaches temperatures close to 950–960 °C [15]. At such high temperatures, aluminum may react with water vapor, introducing hydrogen into the structure and potentially leading to later degradation of the material by IHE. To prevent hydrogen uptake during this process, it is important to maintain a controlled atmosphere [16] or bubble the melt with inert gas or a mixture of inert gas and chlorine [17].

Any manufacturing procedure that involves an aqueous environment poses a potential source of hydrogen. For instance, processes like water quenching or rolling with water-cooled rollers can introduce hydrogen. Additionally, pickling, a common method for removing harmful metallurgical phases through surface treatment, can lead to hydrogen uptake as well [10].

2.1.2. Hydrogen Gas Exposure

The interaction between aluminum and hydrogen becomes significant in applications involving hydrogen storage, such as transportation systems. Aluminum alloys reinforced with carbon fibers are commonly used in hydrogen storage vessels for fuel cell vehicles or industrial applications [12,18]. Storage tanks operating under high-pressure conditions are often filled with liquid hydrogen at pressures ranging from 30 to 70 MPa [12]. The high pressure presents the risk of HE compromising the structural integrity of the storage tanks [19,20]. Molecules of gaseous hydrogen are too large to enter the lattice of any metal; therefore, diffusion is only possible for atomic hydrogen.

Generally, the interaction between a solid and a gas can be described as a series of three processes: physisorption, chemisorption, and absorption. Physisorption works on the principle of weak electrostatic interaction, known as Van der Waals forces. This reversible process easily reaches equilibrium at room temperature and does not include the

reaction of hydrogen [10,21]. The second step, which usually occurs at higher temperatures, is chemisorption. During this process, a covalent bond forms between the dissociated (atomized) absorbed hydrogen gas molecule and the metal surface. Chemisorption involves a chemical interaction over a short distance, taking place in a single atomic layer. Hydrogen dissolution is the third step. Hydrogen diffuses into the material due to the hydrogen concentration gradient [22].

For aluminum, the passive layer of Al_2O_3 does not dissociatively chemisorb atomic hydrogen. The energy barrier is approximately 1 eV/atom. As a consequence, the adsorption rate of hydrogen in dry hydrogen gas at laboratory temperature is low to negligible, showing an increase with temperature and hydrogen pressure, especially above 500 K. Since molecular dihydrogen does not dissociate on Al_2O_3, chemisorption on the aluminum surface requires a direct supply of monoatomic hydrogen [10,23,24].

2.1.3. Corrosion-Induced Hydrogen Uptake

For aluminum and its alloys, hydrogen entry usually occurs in humid conditions when the oxide layer is damaged. For instance, during mechanical loading, when water vapor reacts with the freshly exposed metal surface [25–27], see Equation (1).

Al oxidation in water vapor:

$$2Al + 3H_2O \rightarrow Al_2O_3 + 6H^+ + e^- \quad (1)$$

At the oxide–metal interface, water reduction leads to the formation of chemisorbed atomic hydrogen by a single-electron transfer reaction, known as the Volmer reaction [28]. The mechanism of this process depends on the pH of the aqueous solution [29].

In an acidic solution:

$$H_3O^+ + e^- \rightarrow H_{ads} + H_2O \quad (2)$$

In a neutral or alkaline solution:

$$H_2O + e^- \rightarrow H_{ads} + OH^- \quad (3)$$

Hydrogen produced during corrosion is partly desorbed as molecular hydrogen on the metal surface through chemical recombination (Equation (4)) or electrochemical reactions (Equations (5) and (6)), known as Tafel and Heyrovsky reactions, respectively [10,30].

Tafel reaction:

$$H_{ads} + H_{ads} \rightarrow H_2 \quad (4)$$

Heyrovsky reaction in an acidic solution:

$$H_{ads} + H_3O + e^- \rightarrow H_2 + H_2O \quad (5)$$

Heyrovsky reaction in a neutral or alkaline solution:

$$H_{ads} + H_2O + e^- \rightarrow H_2 + OH^- \quad (6)$$

In parallel with the desorption reaction, atomic hydrogen enters the metal [10,30]:

$$H_{ads} \rightarrow H_{metal} \quad (7)$$

Alloys containing elements with varying nobility are particularly susceptible. When intermetallic particles are more noble than the surrounding aluminum matrix, galvanic coupling occurs, further supporting the corrosion process [31]. Mechanical tests confirm that HE in aluminum alloys might be caused by hydrogen absorbed during corrosion processes [32,33]. Specific examples are mentioned in the chapters on individual aluminum alloys.

2.1.4. Artificial Hydrogen Charging

High-pressure hydrogen gas exposure allows for the introduction of a relatively high amount of hydrogen into the material. This technique requires hydrogen pressure of several MPa and temperature above 500 K for the material to absorb hydrogen. Hydrogen content in materials exposed under these conditions exceeds the equilibrium hydrogen content for atmospheric pressure and temperature [23,24].

Other methods for introducing hydrogen into the metal structure, which can be used to study HE, are plasma gas charging and electrochemical charging [34,35]. In the plasma gas charging technique, hydrogen molecules are converted into H plasma, increasing the hydrogen fugacity and enabling its ingress into the material. This process can be conducted at low temperatures, which is a notable advantage of the technique [36,37]. In the electrochemical charging process, an overpotential is applied to a metal, resulting in a high concentration of hydrogen on the surface [35]. However, there is no single universal technique for electrochemical charging of pure aluminum and its alloys. Various conditions and solutions are used, as described in Table 1.

Table 1. Conditions for electrochemical charging of aluminum and its alloys.

Material	Solution	Current Density [mA·cm^{-2}]	Time [h]	Reference
Al 99.999%	1 N H_2SO_4 + 0.25 g·L^{-1} $NaAsO_2$	50	24	[38]
Al 99.999%	1 N H_2SO_4 + $NaAsO_2$, pH 1, 35 °C	50	24	[39]
5754	3 N HCl	25–300	2	[40]
7050	1 N H_2SO_4 + As_2O_3	20	6–24	[41]
7075	3.5% NaCl	1	NA	[42]
7075	3.5% NaCl + 0.01 N NaOH	1–10	NA	[43]
7085	5% $(NH_4)_2SO_4$	5	480	[44]
7B05-T5	0.1 N HCl + 150 mg·L^{-1} $SC(NH_2)_2$	2	96	[45]
		Potential [V vs. SCE]		
2024	10 mN H_2SO_4	−0.8	40	[46]
2024	10 mN H_2SO_4	−0.8	5–48	[47]
7075	3.5% NaCl	−1.1	NA	[48]
Al–Zn–Mg	H_2SO_4, pH 2	−1.45	72	[49]

NA: Information not available.

2.2. Interaction of Hydrogen with Microstructure

Once hydrogen enters a metal, it diffuses into the material's structure. At room temperature, hydrogen lattice transport in aluminum is very slow [26]. The measured diffusion coefficient of hydrogen in pure aluminum at room temperature ranges from 1.3×10^{-14} to 2.3×10^{-11} m^2·s^{-1} [50–52]. For context, the hydrogen diffusion coefficient for pure iron at the same temperature is 7.5×10^{-5} m^2·s^{-1} [53].

In the crystal lattice, a significant number of defects serve as trap sites for atomic hydrogen [54,55]. These sites are generally divided into reversible and irreversible hydrogen traps, depending on the energy at which the hydrogen is bound [25]. In reversible hydrogen traps, low energy is required to release hydrogen, so it is common for this type of trap to transfer hydrogen to traps with higher binding energy [51]. The release of hydrogen from reversible trapping sites with lower binding energy can be triggered by the application of external stress to the material. Once released, hydrogen becomes diffusible and moves to locations characterized by high-stress fields, where it can initiate the formation of cracks [56]. This is also why these traps are more readily filled, as they retain hydrogen more easily. Unfilled traps pose a barrier to hydrogen diffusion [57,58]. Homogeneously distributed irreversible hydrogen traps could improve resistance to HE by binding hydrogen diffusing through the material [59].

There are three basic structures that act as trapping sites: the crystal lattice, dislocations, and vacancies. The highest energy is required to release hydrogen from vacancies

(desorption energy $E_d = 85 \pm 32$ kJ·mol^{-1}) [51]. While the number of vacancies is low in the absence of hydrogen, it significantly increases with a high hydrogen chemical potential. Vacancies are created during the dissolution of metal and subsequently migrate to surrounding regions. These vacancies accumulate until an equilibrium is reached between vacancy and hydrogen concentrations, ultimately resulting in the formation of a significantly flawed area near the corroding surface [55,60].

Lower energy values are observed for hydrogen traps associated with dislocations ($E_d = 44 \pm 18$ kJ·mol^{-1}). Hydrogen trapped in the crystal lattice exhibits the lowest values of desorption energy ($E_d = 15 \pm 5$ kJ·mol^{-1}). Beyond these primary trapping sites, hydrogen can also be trapped at grain boundaries, near substitutional atoms, or at phase interfaces, including the interface between the precipitate (blue) and the matrix, see Figure 1.

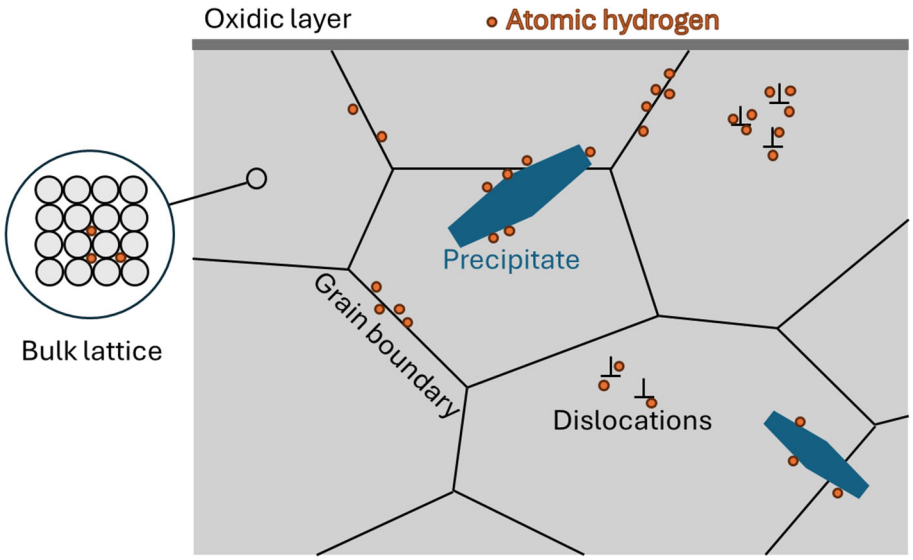

Figure 1. Schematic drawing of trap sites in metals.

Precipitation-hardenable aluminum alloys are characterized by the presence of secondary particles which significantly enhance their mechanical properties [61], see Figure 2. These second phase particles form during heat treatment in a process known as aging [62]. The presence of second phase particles influences hydrogen trapping, depending on properties such as coherency, size, density, distribution, and localization. A critical factor in hydrogen trapping is the phase interface between the precipitate and the matrix. The size of the precipitate is directly related to the amount of hydrogen that can be trapped at the interface [63].

Another crucial property of the interface affecting hydrogen retention is its coherence with the matrix. If the precipitate is coherent with the matrix, it exhibits very high binding energy, acting as an irreversible trap. Hydrogen trapping occurs at the phase interface here. Conversely, incoherent or semi-coherent interfaces lead to hydrogen trapping at misfit dislocations, characterized by a notably low diffusion barrier and serving as reversible hydrogen traps. Such interfaces increase the susceptibility to HE due to weak hydrogen binding [64,65]. The various coherence states are illustrated schematically in Figure 3.

The density of secondary phase particles has a significant effect on hydrogen trapping. A higher concentration of these particles within the matrix corresponds to a greater number of traps available in the material. There are also precipitate-free zones (PFZs) within the material, which exhibit markedly different mechanical and electrochemical responses compared to hydrogen-loaded grain boundaries. Reducing PFZs will mitigate these differences, yielding a positive effect on material performance [32].

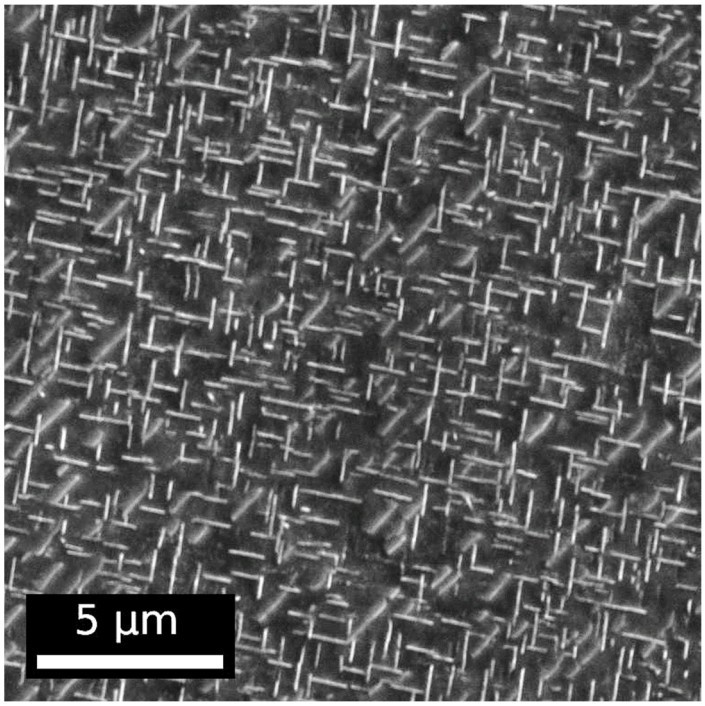

Figure 2. Microstructure of Al-2 wt.% Cu age-hardened alloy.

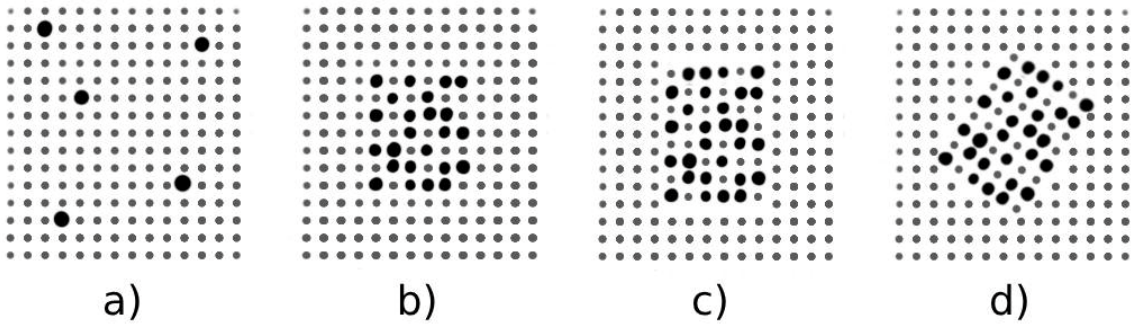

Figure 3. Schematic illustration of: (**a**) solid solution, (**b**) coherent precipitate, (**c**) semi-coherent precipitate, and (**d**) incoherent precipitate. Different size dots indicate different types of atoms.

In addition to density, the uniformity of distribution of the secondary phase particles is of great importance. A denser and more regular distribution enhances hydrogen capture efficiency and reduces the diffusion rate through the material [59]. A specific location where precipitates can be found is at grain boundaries. Here they inhibit the diffusion of hydrogen along grain boundaries, thus modifying the kinetics of hydrogen diffusion [32].

2.3. Mechanisms of HE

The presence of hydrogen within a metallic structure can cause HE, often resulting in severe failure. Currently, four primary mechanisms, besides hybrid mechanisms, for this phenomenon are known. They are discussed in detail by Lynch [11].

The hydride formation mechanism is observed only in environments where hydrides remain stable or become stabilized through a stress field. This phenomenon occurs within specific temperatures and strain rates when hydrogen diffuses into the space behind the crack tip and forms brittle hydrides. This promotes crack propagation, see Figure 4 [11,66].

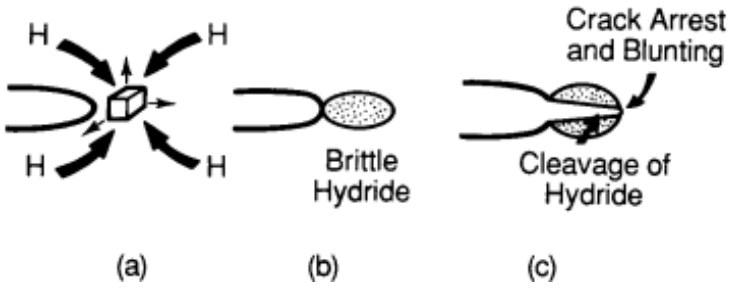

Figure 4. Schematic diagram of hydride formation mechanism. Reprinted with permission from ref. [67], 1989 Elsevier Science Publishing. (**a**) The movement of hydrogen toward areas of elevated hydrostatic stress in front of crack tips. (**b**) Formation of brittle hydride. (**c**) Hydride fracture followed by blunting at the hydride/matrix interface.

Hydrogen-Enhanced Decohesion (HEDE) involves weakening of interatomic bonds due to hydrogen accumulation, resulting in separation of atoms. The process is illustrated in Figure 5. Decohesion is assumed to be a simple, gradual separation of atoms occurring when the critical crack tip displacement is reached, typically around half the interatomic distance [11,25,68].

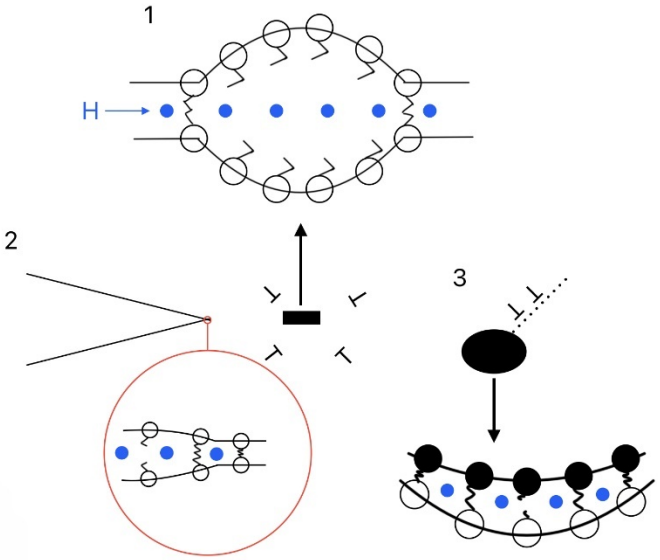

Figure 5. Schematic diagram of Hydrogen-Enhanced Decohesion mechanism. Three types of weakening of the interatomic bond (1) by hydrogen in the lattice (2) by adsorbed hydrogen (3) by hydrogen at the particle/matrix interface. Adapted from Ref. [11].

Hydrogen-Enhanced Localized Plasticity (HELP) involves the interaction of dislocations and hydrogen at the crack tip. Hydrogen reaches the crack tip either through the action of hydrostatic stress or by directly entering the metal structure at the crack, as shown in Figure 6. The movement of dislocations is facilitated by the presence of hydrogen, promoting their rapid propagation and the formation of microcavities that subsequently merge with the growing crack [11,25,66].

In the Adsorption-Induced Dislocation Emission (AIDE) mechanism, hydrogen at the crack tip promotes dislocation emission ahead of the crack tip. It leads to crack propagation through the formation of microvoids, see Figure 7. As a result, small, shallow dimples can be observed on the cleavage-like fracture surface.

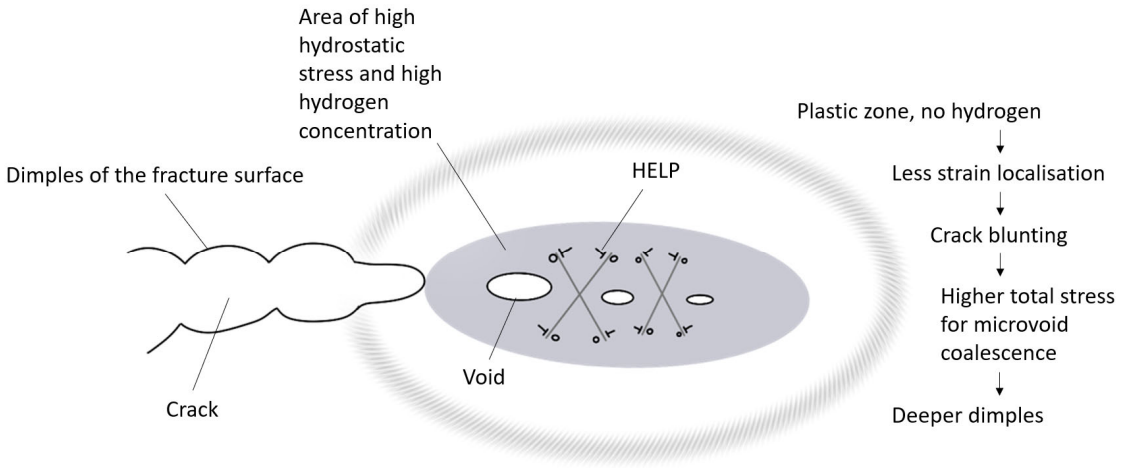

Figure 6. Schematic diagram of Hydrogen-Enhanced Localized Plasticity mechanism. Adapted from Ref. [11].

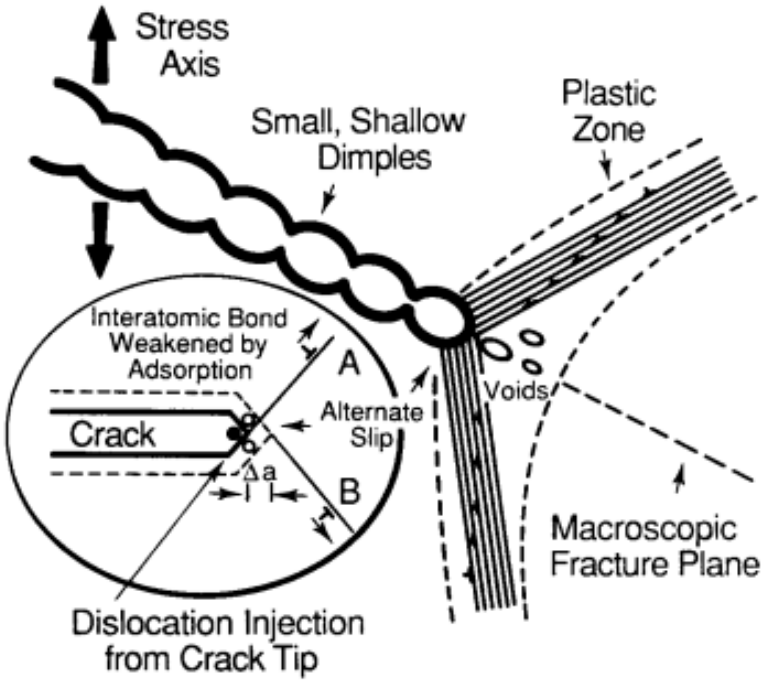

Figure 7. Schematic diagram of Adsorption-Induced Dislocation Emission mechanism. Reprinted with permission from ref. [67], 1989 Elsevier Inc.

Some authors propose that the true mechanism of HE is a combination of the theories mentioned above. Lynch et al. [69] suggested that it is a combination of AIDE and HEDE. The two mechanisms switch according to the current preference for one or the other. AIDE diminishes under stress from ejected dislocations, while it resumes as the crack progresses away from the region of high back stress. Recent theories suggest that HELP is a precursor to HEDE. However, there is no convincing evidence for this combination, as crack growth is usually caused by local plasticity or nanovoid coalescence rather than decohesion [70,71]. At this time, it is not yet possible to identify a preferred mechanism or combination of HE mechanisms for aluminum and its alloys.

2.4. Methods for Hydrogen Detection and Evaluation of HE

Several techniques are employed for hydrogen detection and visualization in aluminum alloys. These include secondary ion mass spectroscopy (SIMS), tritium emission

microscopic autoradiography (TEMA), atom probe tomography (APT), and scanning Kelvin probe (SKP) force microscopy (SKPFM). Meanwhile, thermal desorption analysis (TDA) and electrochemical permeation test (EPT) serve as efficient tools for studying hydrogen diffusion and trapping behavior. For assessing the impact of hydrogen on mechanical performance of aluminum alloys, the primary approach involves conducting a slow strain rate test (SSRT) followed by fractography analysis.

2.4.1. Secondary Ion Mass Spectroscopy

SIMS is a powerful tool utilized for elemental depth profiling in the near-surface layer with high sensitivity and spatial resolution. A sample is bombarded by primary ions from a cesium, oxygen, argon, or gallium ion source. The bombardment leads to the emission of ionized secondary species from the sample surface. These secondary ions are then detected by a mass spectrometer. Detection of hydrogen using SIMS presents several challenges, such as sample contamination by hydrogen-containing species from residual gas in the chamber or instrument background at low mass ranges [72,73]. The capability of SIMS can be improved by detection of hydrogen isotopes, deuterium, or tritium.

Several research groups have utilized SIMS for hydrogen-depth profiling in aluminum and aluminum alloys. Early SIMS experiments proved instrumental in studies related to hydrogen precipitates. For instance, Bond et al. [74] reported a deuterium profile along precipitate in deuterium-charged AA 7050. Rozenak et al. [75] observed a penetration depth of about 1 μm for deuterium after 2 h of chemical and electrochemical charging of pure aluminum. Larignon et al. [76] demonstrated hydrogen-penetration depths of up to 600 μm using SIMS after 72 h of pre-charging of AA 2024.

Interestingly, SIMS did not accurately capture the hydrogen depth profile for pre-charged AA 7075. It detected hydrogen only in the native oxide layer. In contrast, the hydrogen penetration depth revealed by SKPFM varied between 75 and 275 μm, depending on the metallurgical state of the alloy.

Larignon et al. [77] highlighted the limited utility of SIMS in mapping hydrogen absorbed in corrosion defects in AA 2024. In such cases, it is crucial to differentiate the signal of hydrogen trapped in the material and hydrogen originating from corrosion products, particularly hydroxides. To improve accuracy and confirm the presence of hydrogen within the bulk of the material, it is beneficial to use a combination of hydrogen detection techniques.

2.4.2. Tritium Electron Microautoradiography

The TEMA method is used for observation of hydrogen trapping by visualization of tritium distribution at the microscale. The procedure begins with cathodic charging in a solution containing tritium, followed by maintaining the sample at room or slightly freezing temperatures to release excessive hydrogen and achieve an equilibrium distribution of hydrogen. Next, the sample is sectioned into discs, and electrolytic polishing is applied to remove surface film. An emulsion containing AgBr particles sensitive to beta radiation is applied on the sample surface. During several days or weeks of exposure, beta rays emitted from tritium interact with AgBr in the detection layer. This interaction leads to creation of tiny silver particles, which provide information about tritium localization within the microstructure. The spatial distribution of silver is subsequently examined using transmission electron microscopy (TEM).

TEMA has been proven to be a powerful technique for studying hydrogen trapping in various aluminum alloys, such as Al–Cu, Al–Mg–Si, Al–Zn–Mg, and Al–Li [78–80]. Researchers have correlated the distribution of tritium with characteristics of the precipitate-matrix interface, thereby providing valuable insights into hydrogen-microstructure interactions. In addition to the traditional TEMA approach, a tritium release experiment can be conducted to observe hydrogen release from the specimen. In this experiment, the sample is charged in a tritium solution and immersed in a scintillator solution for several hours. The released hydrogen atoms are then revealed by radioactivity detected with a scintillation

counter. Saitoh et al. [81] utilized the tritium release experiment to compare hydrogen trapping efficiency in Al–4Cu and Al–1Mg2Si alloys. Iijima et al. [79] linked changes in the hydrogen trapping efficiency evaluated by this technique with the formation of different precipitates in Al–Zn–Mg alloy.

2.4.3. Atom Probe Tomography

APT allows observation of the precise position of trapped hydrogen atoms. This technique provides perfect chemical and spatial resolution in three dimensions, making it unique among hydrogen detection methods [82]. APT allows for hydrogen detection at interfaces and defects. A needle-shaped specimen with a sharp tip, approximately 100 nm in radius, is prepared using either an electro-polishing procedure or focused ion beam milling. Under ultra-high vacuum conditions, a high positive voltage is applied to the specimen, generating an electrostatic field at its tip. Atoms from the tip are evaporated as ions and accelerated toward a positron-sensitive detector. A cryogenic cooling unit is integrated into the apparatus to suppress thermal atomic vibrations, thereby enhancing APT resolution [82]. However, the use of APT for hydrogen detection presents challenges due to the low mass of hydrogen, resulting in low detection efficiency, and the presence of residual hydrogen in the ultra-high vacuum chamber, which can cause artefacts in the hydrogen signal. Charging samples with deuterium or tritium can help mitigate these challenges.

In studies of aluminum alloys, APT is useful for visualization of hydrogen trapping at the precipitates/matrix interface. He et al. [83] obtained a hydrogen concentration profile from a 3D reconstructed APT image of pre-charged AA 2024, revealing hydrogen segregation at several precipitate interfaces and within particles. Gong et al. [84] reported hydrogen segregation on a second phase interface of AA 7075 in an APT study. Parvizi et al. [85] and Zhao et al. [32] observed effective hydrogen trapping by dispersoid particles in AA 2024 and 7xxx series alloys, respectively. Sun et al. [86] investigated a 7xxx series aluminum alloy, distinguishing particles that act as hydrogen trapping sites from those that do not and observing hydrogen segregation at grain boundaries.

2.4.4. Scanning Kelvin Probe Force Microscopy

SKPFM is a mode of atomic force microscopy (AFM) that combines exceptional spatial resolution (better than 100 nm) with high-sensitivity surface potential measurement, making it capable of hydrogen detection. A conductive cantilever tip vibrates above the sample surface and scans it at a constant distance. The interaction between the tip and sample surface induces a force gradient, which is translated into topography and potential maps. The Kelvin probe technique is based on the principle of compensating for the work function difference between the tip and specimen surface by applying an external bias. Thus, the output of the technique is usually termed the "contact potential difference". SKPFM can be used for hydrogen detection as hydrogen absorbed in the surface layer alters its potential measured by SKPFM.

A palladium layer applied to the sample surface can serve as an effective sensor for absorbing hydrogen desorbed from the specimen due to its high affinity for hydrogen. While some researchers have deposited a palladium layer on aluminum alloy samples studied by SKPFM [64,87], it is not necessary for hydrogen detection. Larignon et al. [76] claimed that diffusing hydrogen destabilizes the natural passive film on the sample surface, affecting electronic output work and consequently the surface potential value. This claim was based on open-circuit potential measurements conducted on hydrogen-charged and hydrogen-free AA 2024 samples.

SKPFM enables local hydrogen detection, particularly detecting hydrogen permeating through grain boundaries or the particle/matrix interface. Safyari et al. [87] observed changes in potential map contrast in an Al–5Mg alloy reinforced by carbon fibers, indicating hydrogen release as the potential difference between the matrix and particle interface increased with time after charging. Larignon et al. [76] demonstrated corrosion-induced hydrogen localization at grain and subgrain boundaries of AA 2024, documented by SKPFM

maps. Another approach used SKPFM to study hydrogen penetration depth in aluminum alloys [47,59,88,89]. The potential measurement was performed perpendicular to the charging side, showing the difference between the potential at a certain distance from the charged side and the potential in the core of the sample. This measurement can be used to evaluate the hydrogen diffusion coefficient. Oger et al. [88] demonstrated the effect of hydrogen trapping by precipitates in aged AA 7046 on hydrogen diffusion depth determined by this method. In their subsequent work [59], they showed that the effect of dislocations on hydrogen penetration depth was less significant compared to the effect of precipitates. Lafouressee et al. [47] utilized the approach and observed hydrogen desorption from AA 2024 samples by measuring the potential gradient evolution of pre-charged samples. The authors reported complete hydrogen desorption after 48 h at room temperature.

2.4.5. Thermal Desorption Analysis

TDA is a general term covering several techniques for analysis of gases released from metals, especially focusing on hydrogen. In TDA, a sample is subjected to controlled heating to induce gradual desorption of hydrogen gas from the material. The heating is conducted under vacuum or in an inert gas atmosphere, typically nitrogen. One common variation of TDA is thermal desorption spectroscopy (TDS), where the released hydrogen flux is ionized and analyzed using a mass spectrometer. The analysis relies on mass-to-charge ratio quantification. Another widely used approach in TDA involves detection of hydrogen effused into carrier nitrogen gas employing a thermal conductivity detector. The amount of hydrogen is quantified based on the difference in conductivity between pure nitrogen flow and the hydrogen–nitrogen mixture. While both methods are widely used for hydrogen desorption studies, detection by mass spectrometer provides superior resolution [90].

The amount of diffusible and trapped hydrogen can be determined by integrating the obtained desorption spectra. Furthermore, analysis of TDA data allows for determination of trap binding energy, trap site density, and concentration of hydrogen in individual trapping sites [64]. In aluminum alloys, TDA is mainly used for hydrogen trapping characterization. The heating rates employed for analysis of trapping sites in aluminum alloys vary from 90 to 1200 °C per hour, see Table 2. Some studies combine non-isothermal heating with an isothermal step to achieve complete hydrogen degassing [91].

Table 2. TDA regimes used for various aluminum alloys.

Alloy	Heating Rate [K·h^{-1}]	Heating Range [°C]	Reference
2024	300	RT–600	[92]
2024	300	RT–600	[28]
2024	600	RT–600	[91,93]
2090	600	RT–600	[49]
2219	100, 200, 300	100–550	[25]
2xxx	200	100–550	[94]
6061	1200	100–570	[27]
7xxx	300	100–550	[9]
7xxx	100, 200, 300	RT–550	[65]
7xxx	120, 240, 360	100–550	[64]
7xxx	100, 200, 300	100–550	[95]
7xxx	960	RT–400	[32]
7xxx	90	RT–550	[63]

RT: Room temperature.

The trap desorption energy is determined from the desorption peak shift towards higher temperatures with increasing heating rates. To ascertain trap desorption energy, the

desorption analysis typically involves measurements under three different heating rates, such as 100, 200, and 300 °C per hour [25,65,94,95]. The evaluation relies on Kissinger's formula:

$$\frac{d\left(ln\left(\frac{\Phi}{T_m^2}\right)\right)}{d\left(\frac{1}{T_m}\right)} = -\frac{E_d}{R} \quad (8)$$

where Φ is the heating rate, T_m is the temperature of the desorption peak, E_d is the desorption energy of each trap site, and R is the gas constant. The desorption energy can be calculated for each peak from the slope of the Arrhenius plot $ln\left(\Phi/T_m^2\right)$ vs. $1/T_m$, known as the Choo–Lee method [96].

TDA is also used for determination of the total hydrogen content [47,59,76,88]. The sample is melted, and hydrogen content is measured using a thermal conductivity detector. The hydrogen content obtained via the melt extraction method is significantly higher than that released by heating below the melting point, typically to 600 °C. Lafouresse et al. [47] compared the total hydrogen content in uncharged and electrochemically pre-charged AA 2024 specimens. The added total hydrogen content varied from 5 to 10 ppm depending on the charging duration.

2.4.6. Electrochemical Permeation Test

EPT can also be used for the determination of hydrogen trapping characteristics, but its primary application is for assessing the hydrogen diffusion coefficient. The method utilizes the Devanathan–Stachurski setup, which consists of two cells with a sample between them acting as a membrane. On one side of the sample, hydrogen entry is induced, typically through cathodic polarization, although immersion in a solution or exposure to humid air inflicting corrosion can also be employed. The hydrogen flow is detected in situ on the opposite side of the membrane by measuring the change in anodic current resulting from oxidation of escaping hydrogen. To prevent corrosion on the hydrogen detection side, it can be palladium or nickel plated. Hydrogen flux as a function of time is obtained. Diffusion and trapping characteristics are evaluated from permeation curves measured until hydrogen flow reaches a steady state. A series of build-up and decay transients may be applied to study hydrogen trapping and detrapping, where reversible trapping sites release hydrogen upon termination of hydrogen entry, while irreversibly trapped hydrogen remains bound.

The diffusion coefficient can be determined using the time lag method, which estimates the diffusion rate based on the delay before hydrogen starts to permeate through the membrane. Alternatively, it can be calculated by fitting the experimental permeation curve to an equation based on Fick's second law [53]. While both methods yield comparable values, the time lag method is more commonly employed.

The employment of EPT for aluminum and aluminum alloys faces several challenges. Even for pure aluminum, a wide range of diffusion coefficient values have been reported, ranging from 10^{-3} to 10^{-7} $cm^2 \cdot s^{-1}$ [52]. Possible reasons for such variation include different testing conditions, sample preparation methods, and the presence of an aluminum oxide layer acting as a barrier for hydrogen transport [97]. Danielson et al. [97] reviewed studies on determining the hydrogen diffusion coefficient in aluminum alloys, reproduced the experiments, and reported corrosion on the hydrogen detection side due to inadequate protective layers. They proposed an improved approach involving optimal palladium deposition and EPT conditions and evaluated hydrogen diffusion coefficients for AA 5083 and AA 6061 alloys. Zheng et al. [98] investigated hydrogen permeation in nickel-plated AA 7075. Ai et al. [99] employed a modified Devanathan–Stachurski test, where the open-circuit potential was monitored on a palladium-coated membrane instead of the permeation current. The authors studied the effect of various degrees of sensitization and orientation on hydrogen diffusivity in AA 5083.

2.4.7. Slow Strain Rate Test

Mechanical testing allows assessment of the susceptibility of materials to HE. The most commonly used technique for this purpose is SSRT. A tensile specimen is mounted in a testing machine and subjected to a constant strain rate, typically ranging from 10^{-7} to 10^{-4} s^{-1}. The specimen can either be pre-charged with hydrogen or exposed to a corrosive environment or pressurized hydrogen gas to induce in situ hydrogen insertion. The low strain rate provides sufficient time for hydrogen accumulation in critical sites. The effect of hydrogen on mechanical properties such as ductility and strength is observed.

The HE index is usually evaluated to compare the characteristics of hydrogen-exposed and reference hydrogen-free specimens. It is calculated using the formula:

$$I_{HE} = \frac{X_{ref} - X_H}{X_{ref}} \cdot 100 \quad (9)$$

where X_{ref} and X_H are selected parameters, typically elongation or reduction of fracture area, for hydrogen-free and hydrogen-charged specimens, respectively. The index is a valuable tool for assessing the impact of hydrogen on material performance.

It is common to use cathodic pre-charging and compare the behavior of uncharged and pre-charged specimens. Several authors have used various durations of cathodic charging and correlated the charging time with the ductility loss of 7xxx specimens, linking it to the increasing amount of absorbed hydrogen [3,41,98,100]. Chen et al. [101] conducted SSRT on Al–Li alloy specimens pre-charged with hydrogen and uncharged specimens. Albrecht et al. [102] conducted SSRT on cathodically pre-charged AA 7075 specimens in a temperature range of −196 °C to 20 °C and reported an increase in the HE effect with decreasing test temperature. Zhao et al. [32] tested specimens pre-charged with both hydrogen and deuterium and observed a similar effect on the mechanical properties of the Al–Zn alloy. Dey et al. [43] chose in situ cathodic hydrogenation at different current densities instead of pre-charging for AA 7075. Krishnan et al. [48] utilized in situ hydrogen charging and compared SSRT results of hydrogenated AA 7010 with those of freely corroding specimens exposed to NaCl solution.

Humid air exposure can also be used to introduce hydrogen into tensile specimens. Safyari et al. [9,64,65] and Moshtaghi et al. [95] evaluated the HE resistance of 7xxx series alloys by conducting SSRT in humid air with relative humidity varying from 60% to 95%, while reference specimens underwent SSRT in dry nitrogen gas. Itoh et al. performed similar experiments on AA 6061 specimens exposed to humid air at 90% RH and dry nitrogen gas [27].

Fractography analysis with scanning electron microscopy is employed to study fracture surfaces after mechanical tests to identify the fracture mode and estimate the corresponding HE mechanism. The transition from ductile dimples to a mixture of dimples with cleavage facets and the shift from transgranular to intergranular mode are typically observed due to the presence of hydrogen in specimens [26,43,48,64,95,100]. Faceted cleavage fracture with secondary cracks might be a sign of a notable hydrogen effect [43]. Additionally, in the case of transgranular ductile fracture, the impact of hydrogen on dimple size can be evaluated [3,102].

3. HE of Various Aluminum Alloys

Aluminum in its pure form is too soft for most practical purposes. Its strength can be increased by adding alloying elements. These alloying elements can increase the strength of aluminum in two different ways: they can replace aluminum atoms in the lattice, forming a substitutional solid solution, or fine particles of secondary phases can precipitate in the alloy microstructure. The former approach leads to hardening through induced strain in the lattice, whereas the latter one causes precipitation hardening [17]. Various heat treatment processes are explained in Table 3. During the first step of precipitation, Guinier–Preston–Bagaryatsky (GPB) or Guinier–Preston (GP) zones are formed. These zones are coherent

with the matrix and increase the strength of the material [17,103–105]. Typically, metastable precipitates with semi-coherent interfaces with the aluminum-based solid solution are formed from these zones. The final over-aged stage is characterized by the formation of stable incoherent precipitates. They enlarge with time, causing a decrease in mechanical properties [62,106–110]. The changes are shown schematically in Figure 8.

Table 3. Heat treating temper codes and their descriptions.

Code	Description	Source
T1	Cooled from an elevated temperature and naturally aged	[111]
T2	Cooled from an elevated temperature, cold worked, and naturally aged	[112]
T3	Solution heat-treated, cold worked, and then naturally aged	[113]
T4	Solution heat-treated and naturally aged to a stable condition	[113]
T5	Cooled from an elevated temperature shaping process and artificially aged	[114]
T6	Solution heat-treated and artificially aged	[113]
T7	Solution heat-treated and over-aged	[113]
T8	Solution heat-treated, cold worked, and artificially aged	[113]
T9	Solution heat-treated, artificially aged, and then cold worked	[113]
T10	Cooled from an elevated temperature, artificially aged, then cold worked	[115]

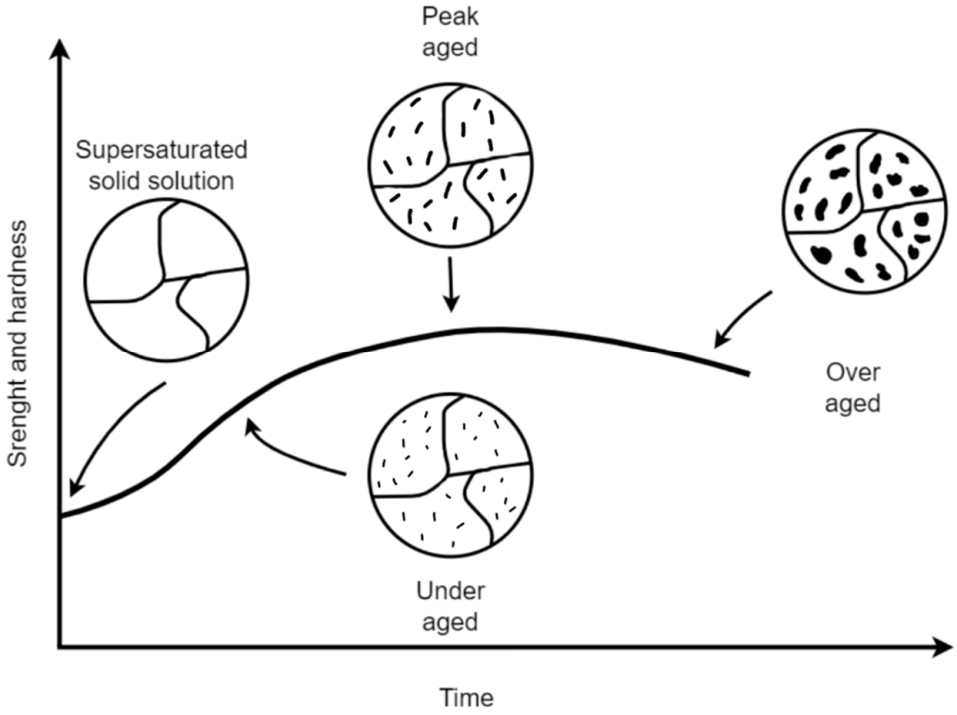

Figure 8. Schematic illustration of aging states of aluminum alloys.

During corrosion, the interface between the precipitates and bulk is prone to hydrogen evolution, which can cause HE. This is due to the different nobility of the alloying elements and the aluminum matrix [30,31,116]. In relation to hydrogen, precipitates can also act as hydrogen traps, where strong trapping reduces the rate of hydrogen diffusion through the material [20,59,88].

3.1. 2xxx Series Alloys (Al–Cu)

3.1.1. Microstructure

The 2xxx AA series consists of aluminum with approximately 4% copper and less than 1.5% magnesium. These materials achieve the desired mechanical properties through a process known as aging, which induces microstructural changes. Among this series, AA 2024 has been extensively studied. Bagaryatsky et al. [117] described a 4-phase precipitation sequence during aging in 1952. It starts with a supersaturated solid solution (SSS), followed by a short-range arrangement of magnesium and copper, termed the Guinier–Preston–Bagaryatsky (GPB) zone [105]. These GPB zones can be understood as clusters of rod-shaped structural units with a diameter below a nanometer [118,119]. The GPB zones dominate the strengthening period over the aging curve. The subsequent phase in the aging process involves the formation of the S″ phase (Al_2CuMg) intermetallic compound, which evolves from the GPB zones to small, fully coherent precipitates [62,107]. The formation of the S phase (Al_2CuMg) is observed during the over-aging period, when softening has already occurred, and exhibits a rod-like morphology in three dimensions and is incoherent with the aluminum matrix [62,106]. Depending on the aging temperature, two different types of S phase particles can form. In solution-treated, quenched, and then cold-worked samples, extensive Type I formation occurs, while Type II formation is inhibited. Type II is characterized as a more stable, non-coherent precipitate with an orientation relationship rotated by approximately 4° compared to Type I. The precipitation sequence can be summarized as follows:

$$\text{SSS} \rightarrow \text{Clusters} \rightarrow \text{S}'' \rightarrow \text{S (Type I)} \rightarrow \text{S (Type II)}$$

Another type of precipitate present in the 2xxx AA series consists of aluminum and copper. It originates from GP zones, which grow to form θ″ (Al_3Cu). During the aging process, θ″ transforms into θ′ (Al_2Cu). In this transformation, some precipitates dissolve, providing additional copper atoms to newly forming precipitates due to the higher copper content present in θ′ compared to θ″ precipitates [120]. At longer aging times or higher temperatures, an equilibrium phase, θ (Al_2Cu), is observed [121].

3.1.2. Corrosion-Induced Hydrogen Entry

Hydrogen entry is closely linked to the process of localized corrosion. The 2xxx series is primarily alloyed with copper, the most noble among the typical alloying elements. The standard potentials of aluminum (−1.662 V vs. SHE) and copper (0.342 V vs. SHE) exhibit significant disparity [122]. Intermetallic particles with notable copper content act as cathodes, contrasting with the surrounding aluminum matrix and inducing local galvanic coupling [116]. The first step of the corrosion process is the release of Al and Mg, leading to the formation of a porous particle structure and an increase in the copper content percentage within the particle [31,116]. Kosari et al. [123] observed this phenomenon after only 30 min of exposure to 0.01 M NaCl, as shown in Figure 9. This process further enhances the cathodic behavior of the particle, and oxygen reduction occurs on its surface. The matrix surrounding the particles becomes increasingly passive; however, a different scenario emerges at their interface. Oxygen reduction on the particle surface induces alkalization, destabilizing the alumina oxide and resulting in the formation of deep trenches around the particle. The dissolution of the matrix can then lead to the separation of S phase particles [31,116]. During the corrosion process, the formation of rings of corrosion products is observed, accompanied by hydrogen evolution and extensive grain boundary attack at these points [30]. Some hydrogen can be absorbed into the material. Localized hydrogen entry is driven by galvanic coupling arising from copper-rich intermetallic particles.

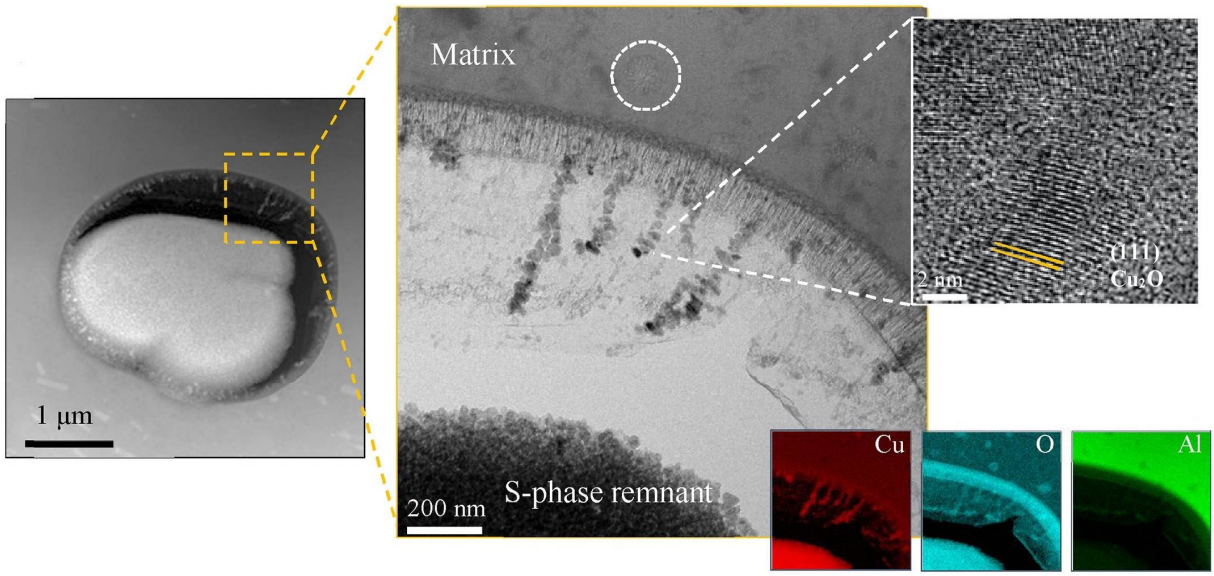

Figure 9. HRTEM image of S phase particle (Al_2CuMg) of AA 2024-T3 exposed in 0.01 M NaCl solution for 30 min. Reprinted with permission from ref. [123]. 2020 Elsevier Ltd.

3.1.3. Hydrogen Interaction with Microstructure

AA 2024 is the subject of extensive study in terms of its interaction with hydrogen. TDS serves as the primary analytical technique, enabling the identification of hydrogen trapping sites based on the temperature at which hydrogen is released.

In AA 2024, TDS detects four primary hydrogen trapping sites, labeled TS1–TS4 based on the temperature of hydrogen release in TDS measurements. According to Kamoutsi et al. [28] and Charitidou et al. [92], the site TS1, characterized by the lowest binding energy, is reversible and associated with hydrogen at interstitial sites. The subsequent sites are considered irreversible. The TS2 site is linked to the semi-coherent interfaces of the strengthening phases or the incoherent interfaces of the dispersoids and the matrix lattice. The formation of Mg hydride is associated with TS3, while the trapping state TS4 is attributed to Al_2CuMg (S phase). However, a recent study by Safyari et al. [94] presents a different perspective on hydrogen trapping phenomena in 2xxx series alloys, particularly in AA 2219. TS1 is associated with hydrogen at interstitial sites. The second peak, TS2, in the TDS spectrum exhibits maximum intensity in cold-rolled specimens with the highest dislocation density near grain boundaries, indicating hydrogen trapped in dislocations. TS3 is associated with hydrogen released from the S′ phase, as evidenced by the peak's presence only in specimens with S′ phase content. The highest binding energy for hydrogen is found in vacancies and grain boundaries. In this study, the last peak in the TDS spectrum, TS4, is linked to the desorption of hydrogen trapped in vacancies, as desorption from grain boundaries requires a higher temperature.

The same research team studied the influence of the coarseness of intermetallic particles, focusing on Al_2Cu particles rather than the S phase. Their findings suggest that particle size significantly affects the quantity of hydrogen they can capture. Moreover, the mechanism of HE is suggested to involve decohesion accompanied by void formation in coarse Al_2Cu particles [25]. These findings are summarized in Table 4.

Table 4. Trapping sites of hydrogen in 2xxx ordered by rising temperature.

Temperature [°C]	Binding Energy [kJ/mol]	Source of Desorbed Hydrogen	Reference
100	NA	Hydrogen at interstitial sites	[10,28,92]
197	NA	Lattice	[25]
200	NA	Semi-coherent phases and dispersoids interface	[92]
209	NA	Hydrogen at interstitial sites	[94]
291	19.30	Al_2Cu fine particles	[25]
374	28.38	Dislocations	[25]
382	15.92	Dislocations	[94]
410	NA	Decomposition of MgH_2	[92,124]
457	40.32	Al_2Cu coarse particles	[25]
458	35.99	S′ phase	[94]
500	NA	S phase	[92,93]
505	50.89	Vacancies	[94]
518	50.89	Vacancies	[25]

NA: Information not available.

During aging, the microstructure of the material gradually changes, as described above. During evolution of second phase particles, their interface with the matrix undergoes changes. GPB zones and S″ precipitates are coherent with the Al matrix, as evidenced by the absence of dislocation strain fields [125]. They are not present during aging at temperatures higher than 250 °C. According to Kamoutsi et al. [91], hydrogen is bound by these trapping sites by stress fields around precipitates. As the microstructure evolves, the precipitates transition from coherent GPB/S″ precipitates to semi-coherent S′ phase and finally to incoherent S precipitates. In the case of incoherent precipitates, it is the interface between the precipitate and the matrix that is responsible for hydrogen trapping [91].

In addition to the S phase, the θ phase also undergoes evolution during heat treatment. Initially, coherent plate-like GP zones are present. As in the case of GPB zones, hydrogen is bound by tensile elastic fields at the particle-matrix interface. Later, plate-like, metastable, and semi-coherent θ′ precipitates evolve from GP zones. The edge of the plate is incoherent with the matrix, while the surface of the plate is coherent with the matrix. The coherency strain is weaker than in the case of GP zones, but incoherent edges can act as hydrogen traps. In the final stage of heat treatment, equilibrium θ precipitates are present. Hydrogen is not trapped by the interface between θ and matrix but by the precipitate itself [80].

A frequently studied aluminum alloy in this series is 2024, which contains manganese or magnesium as alloying elements in addition to copper. He et al. [83] studied the concentration profiles of hydrogen-charged 2024-T3 AA. The results indicated that co-segregation of magnesium and hydrogen occurs when S phase particles are located near grain boundaries. Similar observations of the co-segregation of magnesium and hydrogen have been made at the matrix interface with θ and T phases ($Al_{20}Cu_2Mn_3$).

3.1.4. Effect of Hydrogen on Mechanical Properties

Several studies have reported that exposure of Al alloys to a corrosive environment results in a minor decrease in yield and tensile strength but significant decreases in elongation to failure and strain energy density [62,77,91,126–128]. Mechanical properties tend to deteriorate with prolonged corrosion exposure. Only yield and tensile strength were restored after the mechanical removal of corrosion products, but not ductility. The ductility of the corroded material was restored to its original values after heat treatment. The temperatures employed during the heat treatment were equivalent to the thermal desorption energy of certain hydrogen trap sites [28,33]. This indicates that the reduction in ductility was caused by hydrogen absorbed during corrosion.

The material's susceptibility to HE is closely related to the stage of heat treatment. During the heat treatment process, the microstructure of the material changes fundamentally, as well as the coherence of the forming precipitates. The most studied alloy of the 2xxx series, 2024, was examined in three states of heat treatment. The T3 state, characterized by natural

aging only, is considered an under-aged specimen. The T3 state with additional artificial aging up to the peak-aged condition or over-aged condition was also examined [62,126].

During the under-aged stage, coarse precipitates are not yet formed in the material; however, GPB zones are present. These GPB zones may preferentially develop around grain boundaries, especially in the plastically deformed state. As a result, hydrogen is mainly trapped around the grain boundaries [62,77,129]. Grain boundaries also act as pathways for hydrogen short-circuit diffusion [77]. This explains why the loss of ductility is most pronounced in this state, as the grain boundaries are affected by hydrogen. In the peak-aged stage, S″ and S′ precipitates are formed. They are coherent and semi-coherent with the aluminum matrix. In the case of a coherent interface, hydrogen is captured by stress fields around precipitates. Consequently, minimal ductility loss caused by hydrogen is observed in this stage [62,91]. In the over-aged stage, hydrogen is trapped by the interface between the matrix and incoherent S phase particles, which act as strong hydrogen traps. The fact that the ductility loss is not negligible in over-aged conditions suggests that the coherence of the precipitates is an important factor for hydrogen trapping [62,91]. Table 5 summarizes the changes in mechanical properties induced by hydrogen.

Table 5. Effect of HE in different stages of the aging process in AA 2024.

Heat Treatment Stage	Microstructure State	Ductility Loss	Explanation	Reference
Under-aged	GPB zones	26%	Hydrogen diffusion through grain boundaries, hydrogen traps near grain boundaries	[62,77]
Peak-aged	S′ and S″ phases	11%	Coherent and semi-coherent phases, hydrogen trapped by stress fields around precipitate	[62,91]
Over-aged	S phase	22%	Precipitates incoherent with matrix, strong hydrogen traps	[62,91]

Other authors observed an even stronger loss of ductility. Kermanidis et al. [128] reported a 69% ductility loss after exposure of a sample to an exfoliation corrosion solution for 24 h. Zeides and Roman [127] charged 2024 AA in an ultrasonic bath with 0.1 M NaOH for 840 h, resulting in a 46% ductility loss due to HE. Larignon et al. [130] investigated the effect of hydrogen on the mechanical properties of AA 2024. The relationship between hydrogen content and ductility loss is summarized in Table 6. It is assumed that hydrogen trapped at the interface between the matrix and precipitate relaxes the coherency stresses and reduces local cohesion energy. This facilitates cavity nucleation, leading to lower values of elongation to failure.

Table 6. Hydrogen content in relation to ductility loss of AA 2024 within various times of cathodic charging. Adapted from Ref. [130].

Charging Time	Hydrogen Content	Ductility Loss
7 h	16 wppm	50%
24 h	22 wppm	75%
48 h	27 wppm	70%

3.2. 6xxx Series Alloys (Al–Mg–Si)

3.2.1. Microstructure

The typical 6xxx series alloys are defined by the addition of approximately 0.4 wt.% Mg and 1.0 wt.% Si [131], an alloying ratio required to form Mg_2Si. All alloys within this series are heat treatable, with two primary heat treatment methods, T4 and T6. Both methods begin with dissolution annealing at temperatures above 580 °C, where dissolution of the alloying elements results in the formation of a solid solution. Subsequently, rapid quenching in water prevents precipitate formation, resulting in the alloys treated under the

T4 mode. In the T6 mode, artificial aging occurs at temperatures ranging from 150 °C to 200 °C, leading to precipitate formation. Precipitate strengthening is more important in the 6xxx series than strengthening caused by mechanical deformation [110,132]. The amount of alloying elements not only impacts strength enhancement, but the addition of Si, Cu, and Ag accelerates age-hardening kinetics [133].

At the beginning of the aging process, a supersaturated solid solution forms as a result of the rapid cooling process during quenching. The first step is the formation of Si and Mg clusters [104], as seen in Figure 10a. It is suggested that the clustering process is controlled by the migration of Si and Mg [133]. These clusters then form GP zones, which consist of Mg–Si co-clusters [104]. The primary precipitates, known as β″ (beta double prime) Mg_5Si_6, are shown in Figure 10b. They are coherent with the matrix and rod-shaped. Dense dispersion of these precipitates enhances mechanical properties [110]. Over-aging, beyond the peak hardness level, leads to the transformation of β″ into several other metastable phases, such as β′, B′, U1, and U2 [132]. It is assumed that β′ is easier to precipitate than other metastable phases, and an excess of Si also facilitates the formation of this type of precipitate [134]. The final stage of precipitation evolution involves the formation of incoherent precipitates β (Figure 10c), which are a characteristic feature of over-aged conditions and are associated with diminished mechanical properties [109,110]. The addition of Cu (0.5 wt.%) as an alloying element improves mechanical properties by introducing a new type of precipitate particle known as Q′. Q′ is based on the quaternary equilibrium phase Q ($AI_5Cu_2Mg_6Si_6$) phase. Together with β′, Q′ plays a significant role in improving mechanical properties [109,135–137].

3.2.2. Hydrogen Embrittlement

Compared to other reviewed types of aluminum alloy, the 6xxx series alloys are considered to have good HE resistance [27,138]. This is confirmed by several mechanical tests comparing samples exposed to a hydrogen source and a reference, as shown in Table 7. However, they are not completely immune. Itoh et al. [27] demonstrated that alloy 6061 with high Si content is susceptible to hydrogen when exposed to humid air at 90% RH. Osaki et al. [139] also exposed samples from the 6xxx series (0.7 wt.% Mg, 1.1 wt.% Si) to high humidity and observed a loss of mechanical properties, although relatively minor. Intermetallic particles $(Fe,Mn,Cr)_3SiAl_{12}$ had the greatest impact on hydrogen trapping. The particles possess extremely high desorption energy compared to other trapping sites, effectively hindering hydrogen diffusion deep into the material [20]. This blocking effect is clearly visible in Figure 11, where the occurrence of hydrogen can be observed precisely in regions with elevated concentrations of iron, silicon, and chromium. The more concentrated occurrence of these elements indicates the presence of secondary particles. Hydrogen trapped by second phase particles and microvoids can be detected in the TDS spectrum within the temperature range of 470 °C to 560 °C, where a peak appears regardless of environmental humidity. Hydrogen desorption can also be observed at lower temperatures, corresponding to the release of hydrogen from dislocations [27].

Table 7. Ductility loss of 6xxx series aluminum alloys after exposure to a source of hydrogen.

Material	Ductility Loss	Reference
6061	7%	[138]
6070	7%	[138]
6013	7%	[138]
6066	13%	[138]
6061 0.1% Fe	18%	[140]
6062 0.2% Fe	none	[140]
6063 0.7% Fe	none	[140]
6xxx (0.7 wt.% Mg, 1.1 wt.% Si)	17%	[139]

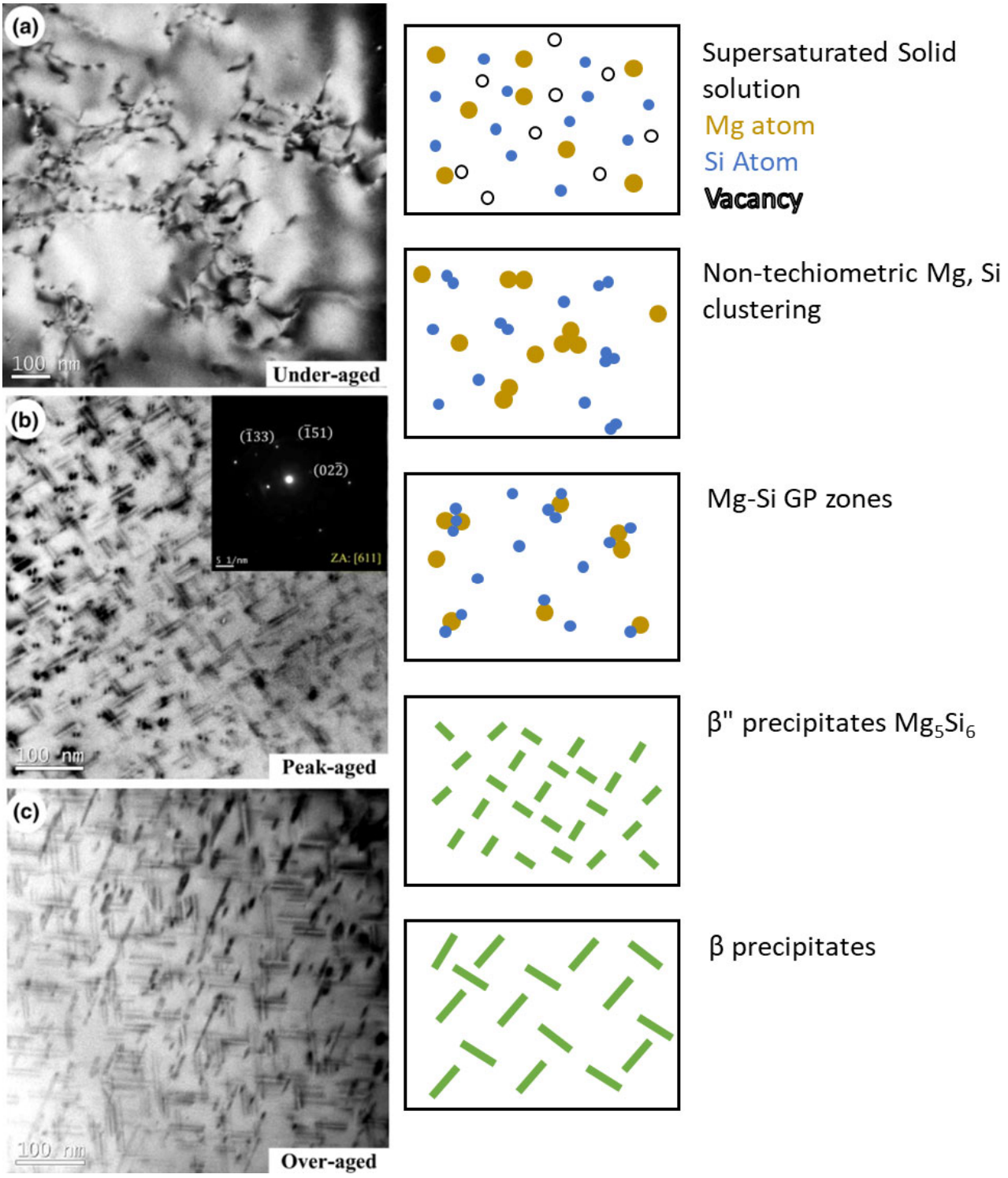

Figure 10. TEM (bright field) images of AA 6063 in: (**a**) under-aged, (**b**) peak-aged, and (**c**) over-aged conditions. Adapted from Ref. [104].

During the aging process, the microstructure of the material undergoes a gradual change. During the evolution of second phase particles, the interface between the particles and the matrix also evolves, as does the way in which hydrogen is captured. Saitoh et al. [80] investigated this process using tritium electron microautoradiography. Initially, needle-like GP zones are present, which lack the ability to trap hydrogen. Hydrogen is repelled by compressive elastic fields surrounding GP zones. This phenomenon is known

as the Gorsky effect, whereby dissolved hydrogen in metal crystals moves from a region with compressive elastic stress fields to a region with tensile elastic stress fields. In the later stages of the aging process, β′ precipitates are present. In this case, hydrogen is trapped at the interface between the β′ precipitates and the matrix. This interface contains dislocations that act as hydrogen trapping sites. In the final over-aged stage, β precipitates form. Due to their incoherency, numerous dislocations appear at the interface between the β precipitates and the aluminum matrix, accumulating trapped hydrogen.

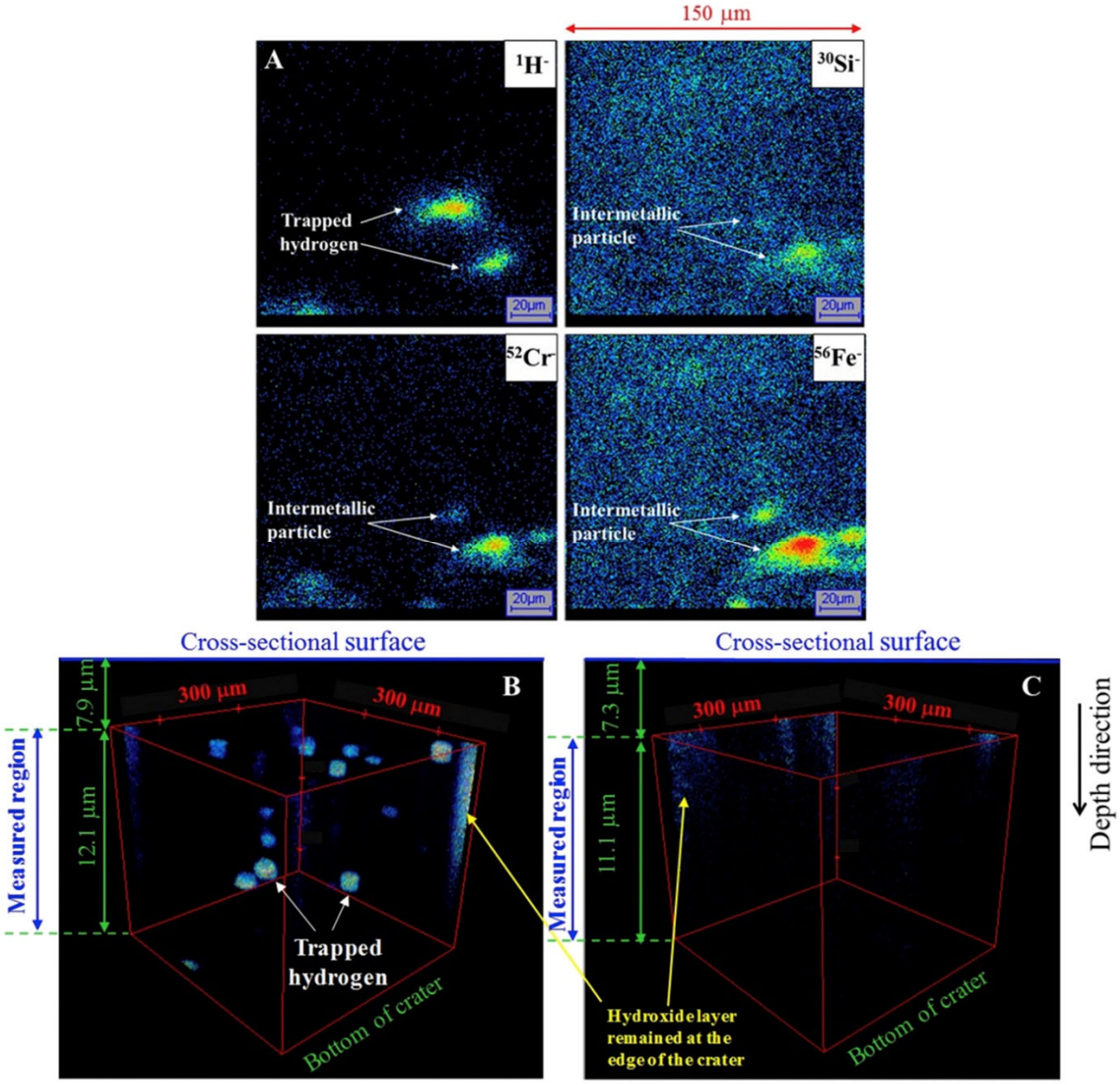

Figure 11. Imaging of hydrogen trapped in a sample of AA 6061-T6 charged with hydrogen using both two-dimensional (2D) and three-dimensional (3D) secondary ion mass spectrometry (SIMS). Reprinted with permission from ref. [20], 2017 Hydrogen Energy Publications LLC. Published by Elsevier Ltd. (**A**) 2D images of $^{1}H^{-}$, and $^{28}Si^{-}$, $^{52}Cr^{-}$, $^{56}Fe^{-}$ (**B**) 3D image of $^{1}H^{-}$ (**C**) 3D image of $^{1}H^{-}$ after TDA measurement.

Even a minor change in the composition of aluminum alloy could make a significant difference. In Al–Mg–Si systems, the inclusion of minor quantities of iron (ranging from 0.1 to 0.7 wt.%) can inhibit HE by trapping hydrogen within the Fe–Si intermetallic [140]. As illustrated in Figure 11, intermetallic particles containing Si, Cr, and Fe elements exhibit the highest concentration of trapped hydrogen [20]. In contrast to Fe, a higher Si content

(0.81 wt.%) without excess Mg addition increases the sensitivity of 6xxx alloys to HE. This is probably due to the reaction between aluminum and water vapor to produce hydrogen, which penetrates into the sample and accumulates on the Si-rich phase at grain boundaries. This accumulation leads to a reduction in interface strength with the matrix phase [138].

Due to the presence of coherent or semi-coherent interfaces of precipitates, there are increased free volumes or local lattice distortions. These features could act as hydrogen traps and affect the cohesion energy. Therefore, HEDE is considered a model for HE [141].

3.3. 7xxx Series Alloys (Al–Mg–Zn)

3.3.1. Microstructure

The characteristic alloying components for the 7xxx aluminum alloy series are zinc and magnesium. Additionally, other alloying elements such as copper, manganese, silicon, magnesium, zinc, zirconium, nickel, cesium, cobalt, and iron can be added [4]. These alloying elements lead to the formation of several types of precipitated phases [142].

The primary alloying elements form precipitates η ($MgZn_2$), which are sometimes referred to as "M" precipitates [108]. The precursor to these precipitates is η′ ($MgZn_2$), which serves as the primary strengthening phase in this alloy series. Another notable phase is $Al_2Mg_3Zn_3$, known as the T phase. Copper addition increases the number of precipitated η′ phases, thereby enhancing tensile strength and elongation. Furthermore, the presence of copper allows the formation of Al_2Cu θ or S′ and S phase particles, which are described in more detail in the chapter on 2xxx aluminum alloys [4,142,143]. The presence of chromium in the 7xxx AA series leads to the formation of E-phase $Al_{18}Mg_3Cr_2$ precipitates [84].

The fraction of precipitating phases is significantly affected by the specific cooling path followed during solidification. This dependence indicates that modifying the cooling conditions can result in the formation of different amounts of precipitating phases within the material. Figure 12 illustrates how the equilibrium fraction of these phases changes with temperature.

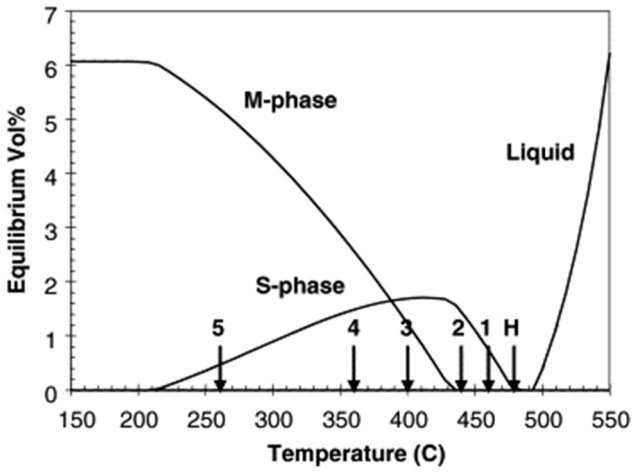

Figure 12. Changes in equilibrium fraction of precipitating phases in AA 7050 in relation to temperature; H: homogenization temperature, 1 to 5: various quenching temperatures. Reprinted with permission from ref. [108], 2004 Elsevier B.V.

3.3.2. Hydrogen Interaction with Microstructure

The 7xxx series are notable for their superior mechanical properties. However, this advantage comes at a cost due to their susceptibility to hydrogen-induced failures [144]. Already in 1974 it was reported by Gest and Troiano that HE contributes to the stress corrosion cracking process of 7075 aluminum alloy [145]. Further studies have confirmed that the presence of hydrogen in 7xxx alloys results in both brittle transgranular and intergranular fractures [33,59,144,146]. The content of brittle fractures is found to increase as the hydrogen content rises, as evidenced by Figure 13 [41]. An increasing degree of

brittle fracture is manifested by a reduction in the number of dimples, which are typically associated with plastic deformation.

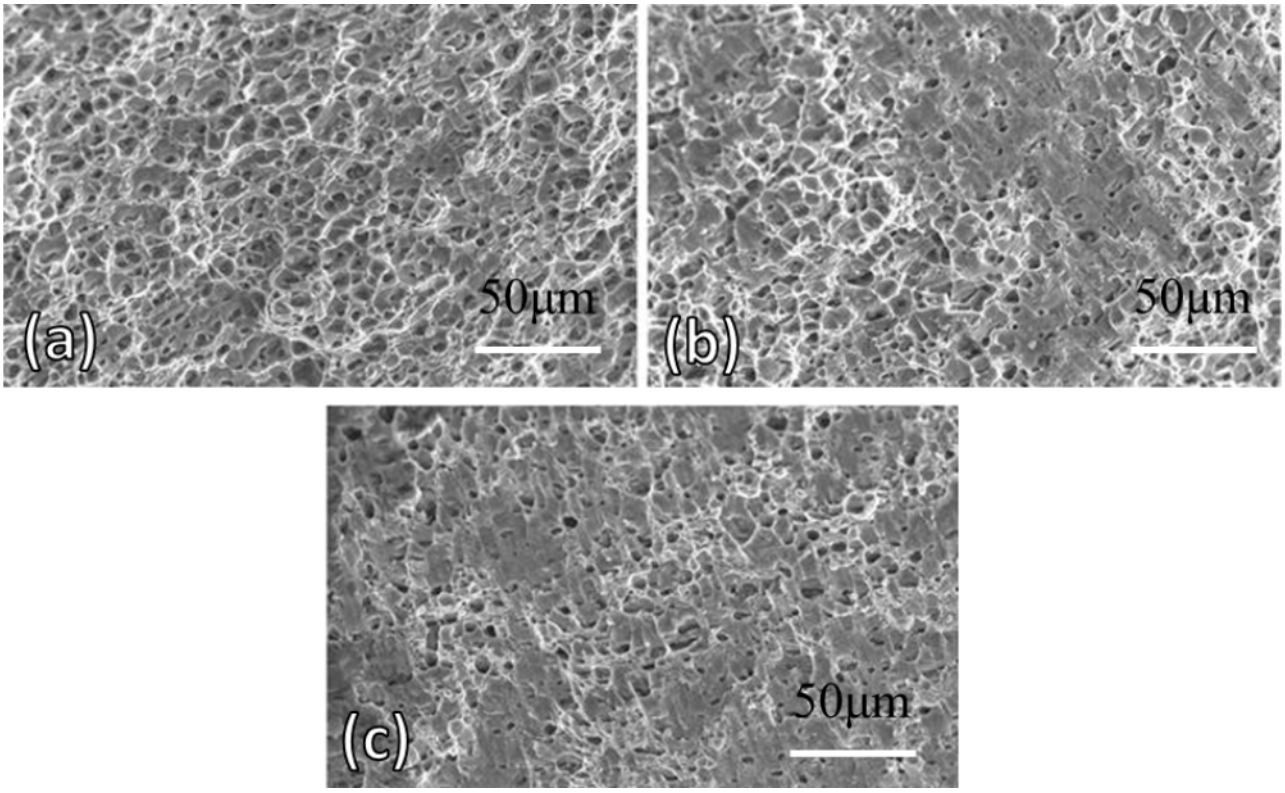

Figure 13. Fracture surface of the 7050 aluminum alloy in three different states: (**a**) in air, (**b**) precharged with hydrogen for 12 h, and (**c**) 24 h. Reprinted from ref. [41], 2015 ASM International.

The phenomenon of hydrogen trapping in precipitated particles, as described in the chapter on the 6xxx series, is also observed in the 7xxx series. The presence of precipitates reduces the diffusion rate of hydrogen into the material [59,88]. Figure 14 shows that in the absence of η-$MgZn_2$, a typical second phase for 7xxx series aluminum alloys, hydrogen tends to be captured at grain boundaries and dislocations. In the presence of precipitates, hydrogen penetration into the material is impeded because the precipitates act as strong hydrogen traps [59]. This claim is supported by a study conducted by Zhao et al. [32], which argues that in the initial stage of HE, hydrogen primarily accumulates on intermetallic phases rather than in the matrix or (Mg–Zn)-rich precipitates. At this stage, the material exhibits low susceptibility to HE. However, if saturation of these primary trapping sites occurs, hydrogen becomes trapped at grain boundaries. At this stage, the presence of magnesium further enhances the affinity of hydrogen for grain boundary deposition. This can result in grain boundary decohesion and crack formation [32,100]. As outlined by Sun et al. [86], when zinc clusters form at grain boundaries, an increased concentration of hydrogen is observed. This indicates that the presence of zinc in the material could cause segregation of hydrogen at grain boundaries. Figure 14b shows that in materials with precipitates, hydrogen is concentrated closer to the surface than in materials without precipitates, see Figure 14a. In the study, second phase particles formation in 7046-T4 aluminum alloy was achieved by additional artificial aging for 20 h at a temperature of 150 °C [59]. The addition of chromium, which causes formation of the E-phase, resulted in significant segregation of hydrogen between this phase and the matrix. This behavior could lead to a higher susceptibility to HE in this grade [84].

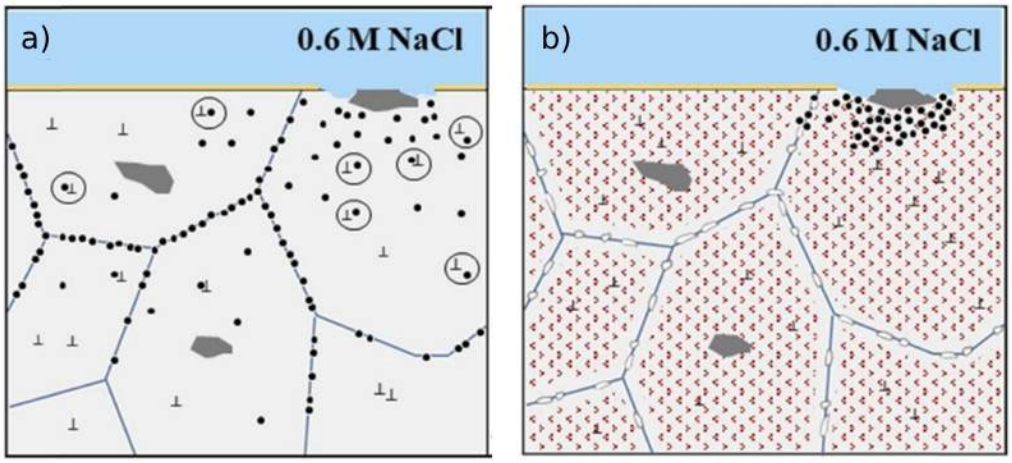

Figure 14. Schematic illustrations of different hydrogen diffusion in AA 7046-T4: (**a**) without and (**b**) with intragranular η-$MgZn_2$ precipitates (red dots). Reprinted with permission from ref. [59], 2022 Elsevier B.V.

During the aging process, second phase particles evolve continuously. They change properties such as stability, geometry or coherence with the matrix. These properties are closely related to the hydrogen trapping mechanism. In the early stages of aging, spherical GP zones are present. The particles are coherent with the matrix and exhibit a compressive elastic stress field, due to the Gorsky effect, which describes the movement of hydrogen in metal crystals from a region with compressive elastic stress fields to a region with tensile elastic stress fields. GP zones have been observed to repel hydrogen. Plate-like, metastable, and coherent η′ precipitates form from GP zones. Due to their coherence and the absence of a stress field around the precipitates, they do not trap hydrogen. In the over-aged state, rod-like equilibrium and incoherent η precipitates form. Incoherence with the aluminum matrix results in an increase in hydrogen trapping capacity around the precipitates in over-aged material [79].

3.3.3. Effect of Hydrogen on Mechanical Properties

The 7xxx aluminum alloys susceptibility to HE is significantly affected by heat treatment [147]. Various heat treatment regimens result in distinct microstructures, leading to varying degrees of susceptibility to HE in 7075 aluminum alloy, as outlined in Table 8. The impact on HE diminishes with increasing aging time. There is also a visible correlation between the coherence of precipitates and their effect on HE. The greatest effect is observed in the under-aged state with coherent GP zones, while the effect is the lowest in the over-aged state with semi-coherent precipitates. This dependence is demonstrated by comparing the reduction of the fraction area in Table 9. Upon lowering the test temperature from 20 °C to −98 °C, the HE effect increases significantly for the over-aged state, whereas HE susceptibility of the under-aged state shows no temperature dependence [102].

For 7050 AA, Qi et al. [41] showed the same trend, see Figure 15. Hydrogen had the highest influence on degradation of mechanical properties in the under-aged state, while it was the lowest for the over-aged and medium for the peak-aged states. Takano [148] observed a severe decrease in elongation to fracture and tensile strength of 7075 AA.

Table 8. Effect of different stages of the aging process on HE in AA 7075. Adapted from Ref. [102].

Heat Treatment Stage	Microstructure State	Effect on HE	Explanation
Under-aged	GP zones (coherent precipitates) at grain boundaries	Largest	Passing dislocations can cut GP zones, local softening, formation of concentrated slip bands
Peak-aged	Mixture of GP zones and η′; η at grain boundaries; precipitate-free zones formation	Moderate	Mixture of GP zones and semi-coherent precipitates causes non-homogeneous slip distribution; homogeneity improves with increasing strain
Over-aged	Coarse η′ particles in matrix; large η and T-phase at grain boundaries; growth of precipitate-free zones	Smallest	Semi-coherent precipitates result in a homogeneous slip distribution

Table 9. Percentage reduction of fraction area in tensile tests for hydrogen-charged and reference samples of AA 7075. Adapted from Ref. [102].

	Under-Aged	Peak-Aged	Over-Aged
Uncharged [%]	28	29	33
Charged [%]	15	20	28
Difference [%]	48	30	16

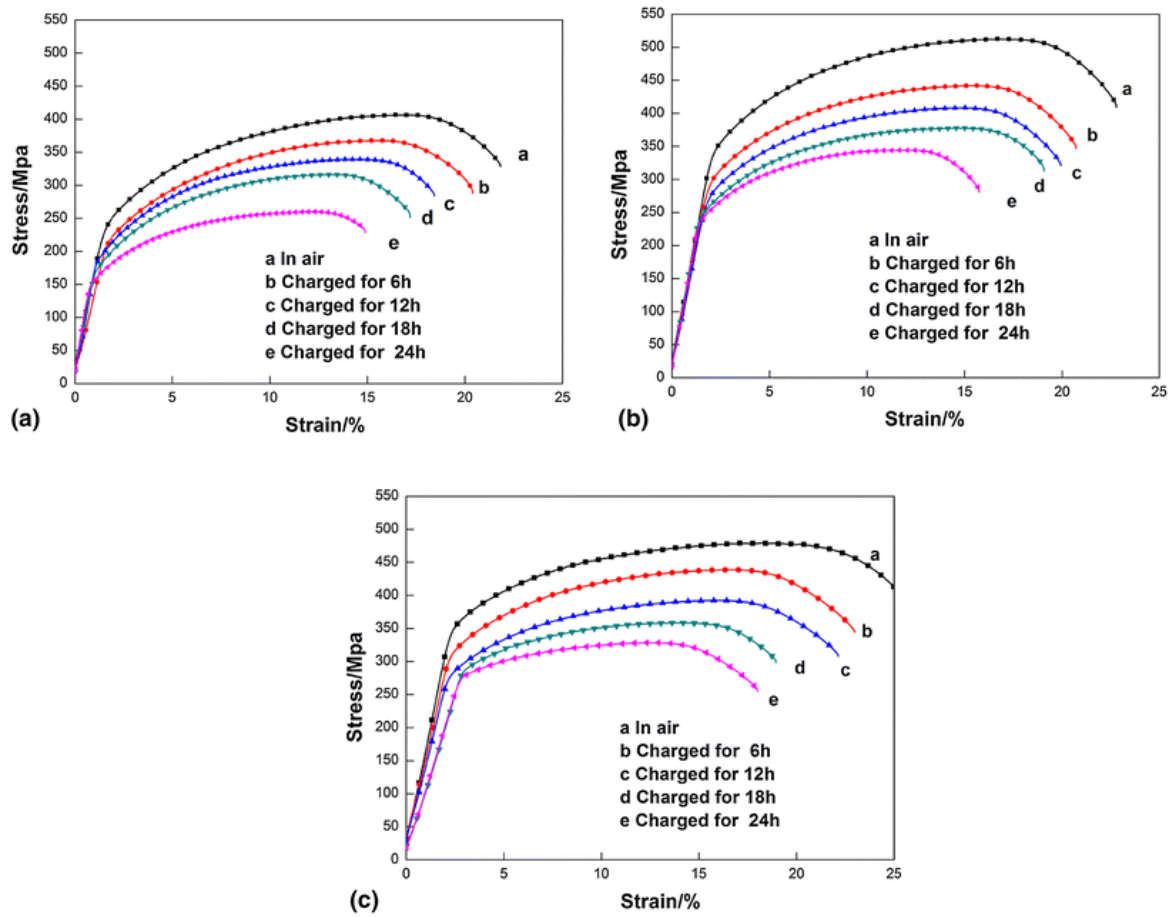

Figure 15. Stress-strain curves of: (**a**) under-aged, (**b**) peak-aged, and (**c**) over-aged condition of AA 7050 with different charging times. Reprinted from ref. [41], 2015 ASM International.

Kumar and Namboodhiri [3] conducted a study to evaluate the susceptibility of AA 7020 to HE using different cooling techniques after solution annealing at 480 °C, namely water quenching or air cooling. Samples quenched in water exhibited greater hardness compared to those that were air-cooled, but they also displayed increased vulnerability to HE [3]. It is noticeable that HE is only present in the alloys quenched in water, as indicated in Table 10. Solution treatment and quenching are crucial as they anneal mechanically deformed surfaces (e.g., after polishing and grinding). These surfaces contain a high number of dislocations that could affect hydrogen permeability and transport through mobile dislocations [149–151]. Dislocations also offer a protective effect against HE, according to Oger et al. [89]. An increase in dislocation density correlates with a reduction in HE susceptibility. The effect has been attributed to hydrogen trapping by dislocations, limiting its diffusion and reducing the amount of hydrogen trapped in grain boundaries. A high concentration of hydrogen at locations with high dislocation density, mainly behind the crack tip, leads to the expansion of the plastic zone. Under these circumstances, the assumed mechanism of HE for 7xxx alloys is HELP [7]. The HELP mechanism is frequently referenced in the literature due to the presence of microvoids on a small fraction of the fracture surface [48,95]. Additionally, Aboura et al. [152] proposed that, besides the HELP mechanism, environmentally assisted transgranular cracking observed in their experiment could be explained by the AIDE mechanism. Bal et al. [153] put forth the hypothesis that HELP and HEDE coexist in aluminum alloy 7075. The prevailing mechanism is temperature-dependent, with the HELP mechanism prevailing at elevated temperatures (100 °C). Furthermore, numerous authors also tend to favor the HEDE mechanism, where hydrogen affects the coherent energy of the grain boundaries and precipitate interfaces [3,9,32,64,154]. Given the range of opinions within the scientific community, it is likely that the mechanism for this type of alloy will be a complex combination of the above mechanisms, dependent on ambient conditions and specific alloy composition.

Table 10. Maximum strain during tensile test at strain rate 10^{-5}/s for AA 7020. Adapted from Ref. [3].

	Air Cooled	**Water Quenched**
Uncharged	0.19	0.19
Charged	0.19	0.14
Difference [%]	0	26

3.4. Al–Li Alloys

3.4.1. Microstructure

Aluminum–lithium (Al–Li) alloys are promising materials for aerospace applications due to their enhanced stiffness and reduced density compared to conventional aluminum alloys [155]. In aluminum alloys containing more than 1 wt.% lithium, metastable and coherent precipitates δ′ Al_3Li emerge. When these precipitates are homogeneously distributed, mechanical properties are significantly improved [156]. For instance, the peak-aged condition of AA 8090 was measured after 40 h of aging at 190 °C [157], as shown in Figure 16C. The precursor for δ′ are GP zones and δ″ phase [103,158]. After reaching the over-aged phase, heterogeneous precipitation of the equilibrium phase δ AlLi occurs. Heterogeneous nucleation takes place at grain boundaries, resulting in lithium-depleted, precipitate-free zones (PFZs) near grain boundaries [103,156]. The space between the δ′ precipitates increases with aging time, while the δ′-PZF around grain boundaries becomes wider with aging time, see Figure 16 [157].

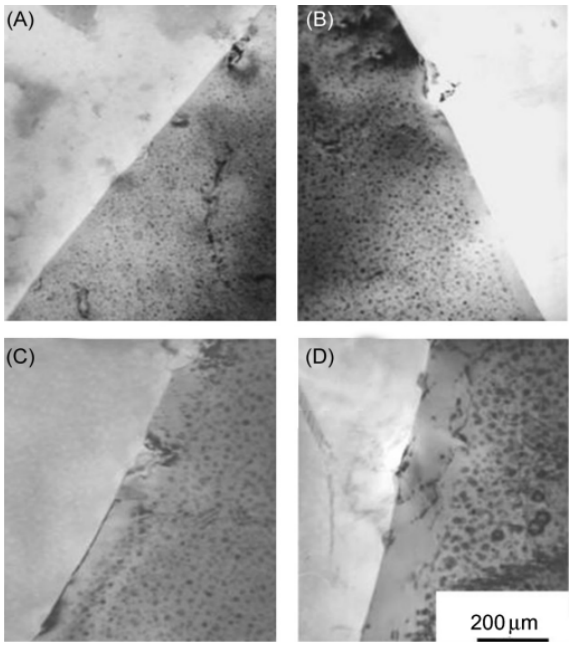

Figure 16. TEM images of Al–Li alloy 8090 at different stages of aging at 190 °C: (**A**) after 1.5 h, (**B**) 10 h, (**C**) 40 h, and (**D**) 100 h. Reprinted with permission from ref. [157], 2014 Elsevier Inc.

Crucial alloying elements in Al–Li alloys are magnesium, copper, and zirconium. Magnesium promotes δ′ precipitation and participates in the formation of precipitate T Al_2MgLi in over-aged conditions. Copper contributes to the formation of θ′ Al_2Cu_2, particularly when the Cu:Li ratio exceeds 1:3 (wt.). Copper is also present in T1 Al_2CuLi. Zirconium inhibits recrystallization and forms β′ Al_3Zr precipitates [103].

3.4.2. Hydrogen Embrittlement

Lithium has a distinct property among alloying elements in aluminum alloys due to a high affinity for hydrogen. Consequently, Al–Li alloys can accommodate up to ten times more dissolved hydrogen than other aluminum alloy series. The main source of hydrogen absorption is the contact of Al–Li alloys with atmospheric moisture during melting [156,159].

δ′ precipitates act as hydrogen traps only when they are coherent and metastable. Semi-coherent metastable δ′ does not act as a trapping site for hydrogen. In the case of equilibrium δ precipitates, hydrogen is trapped at the incoherent interface between δ and the matrix by interfacial dislocations. It is important to note that dislocations act as trapping sites for hydrogen and also as short-circuit paths for hydrogen diffusion [78].

Trapping energies of microstructural features found in Al–Li alloys are summarized in Table 11. The binding energy of δ′ Al_3Li precipitates is lower than that of precipitates formed in the presence of copper, T1 Al_2CuLi [49]. T1 precipitates facilitate hydrogen entry to the material structure. One possible explanation is that the T1 phase exhibits a low hydrogen overpotential. The hydrogen reduction reaction then occurs on the copper atomic layers within the precipitate structure. Subsequently, hydrogen is free to diffuse along the T1–matrix interface. At the same time, precipitates strongly bind hydrogen due to their high binding energy, reducing HE susceptibility, as hydrogen is trapped inside the T1 precipitates rather than at phase interfaces. The trapping capacity suppresses hydrogen diffusion to the grain boundaries, which also contributes to high HE resistance [49,160,161].

Table 11. Trapping energies of microstructural features in Al–Li AA. Adapted from Ref. [49].

Trapping Site	Binding Energy [kJ/mol]
Interstitial	0.0
Li in solid solution	2.6
δ'	25.2
Dislocations	31.7
High-angle grain boundaries	35.0
T1	38.0

The microstructure of a material has a significant impact on its susceptibility to HE. The best resistance to HE is typically observed when the material is in the peak-aged condition, likely due to the ideal distribution of δ' in the matrix. If the aging time is too long and transformation of δ' or θ' precipitates to T1 occurs, strain is induced at grain boundaries. This leads to an increase in the critical concentration of hydrogen, resulting in a higher susceptibility to HE compared to the peak-aged condition. Al–Li alloys in under-aged condition are highly susceptible to planar slip, which facilitates the transport of hydrogen and increases the exposed surface area of the material by producing numerous slip steps. The increase in exposed surface area provides additional sites for hydrogen reduction to occur, promoting hydrogen ingress into the material [162]. A summary can be found in Table 12.

Table 12. Effect of different stages of the aging process in Al–Li alloy (2.30% Li, 1.24% Cu, 0.80% Mg, 0.12% Zr) on ductility loss. Adapted from Ref. [162].

Heat Treatment Stage	Ductility Loss	Short Explanation
Under-aged	25%	Planar slip favors hydrogen transport by dislocations and also causes an increase in the surface area
Peak-aged	17%	Optimum distribution of δ' phase, which acts as a strong hydrogen trap
Over-aged	23%	Strain on GB developed, leading to an increase in the critical concentration of hydrogen

The susceptibility of Al–Li alloy to HE was also examined by Chen et al. [101] through mechanical testing and fracture analysis. A notable effect of hydrogen on the ultimate tensile strength and yield strength was evident at slower strain rates. The hydrogen-saturated samples also showed a significant decrease in plasticity. This was further confirmed by fracture investigations, where at a higher strain rate of 3.4×10^{-3} s^{-1}, ductile fracture occurred at grain boundaries, whereas at lower strain rates of 3.4×10^{-4} and 3.4×10^{-5} s^{-1}), brittle fracture at grain boundaries was observed. When the strain rate is slow and excessive hydrogen is present (hydrogen-charged sample), dislocation core atmospheres form as a result of hydrogen–dislocation interactions. Hydrogen is then carried into the PFZ, causing cracking and enhancing dislocation slip on the slip plane in the PFZ.

4. Current Knowledge and Challenges of Future Research

4.1. Mechanism of HE of Aluminum Alloys

The mechanism of hydrogen embrittlement (HE) in aluminum alloys is a topic of ongoing research, with several competing theories. Nevertheless, further evidence is required to substantiate the involvement of a specific mechanism. This would assist in determining whether a single process or a combination of mechanisms is responsible for HE in these materials.

As mentioned in Section 2.3, recent research by Lynch et al. [69] suggests that HE is a combination of HEDE and AIDE mechanisms. Scully et al. [10] lean towards the HEDE mechanism. The presence of precipitates, specifically $MgZn_2$, also contributes to HE via this mechanism. During the oxidation of the aluminum surface, vacancies are injected,

as aluminum atoms leave their positions to form the oxide layer. These vacancies, in combination with the high trapping capacity of the precipitates, result in the concentration of hydrogen in the surface layer. Hydrogen then can diffuse to the crack tip, where its accumulation leads to an enhanced rate of crack propagation.

The lack of convincing studies is attributed to the low lattice solubility of hydrogen in aluminum alloys, which complicates hydrogen quantification [10]. Advanced, sensitive techniques are required to detect these low hydrogen concentrations and further our understanding of HE. Consequently, elucidating the mechanism of HE of aluminum alloys depends on current research studies.

4.2. Investigation of HE of Aluminum Alloys

Research on HE in aluminum alloys includes the process of saturating the metal with hydrogen. Artificial hydrogen charging methods aim to achieve a specific distribution and concentration of absorbed hydrogen within the alloy. However, variability in these methods, particularly in electrochemical hydrogen charging conditions, introduces challenges in achieving consistent results.

Another critical aspect is hydrogen content measurement. While most researchers focus on determining the distribution of hydrogen within various trapping sites using TDA, accurate hydrogen concentration data are also crucial. For instance, a significant gap remains in understanding the critical hydrogen content needed to induce HE under different stress levels in aluminum alloys. Unlike steel, there is no consensus on standardized approaches for measuring hydrogen content in aluminum alloys, and distinguishing between reversible and irreversible hydrogen trapping is still not well-defined. The total hydrogen content is often reported in studies; however, it is more critical to identify the proportion of diffusible hydrogen that contributes to crack initiation and propagation. In contrast, irreversible hydrogen trapping can actually reduce susceptibility to HE by preventing hydrogen from reaching critical areas. Therefore, it is essential to study the trapping capacity of various microstructural constituents, including precipitates, to accurately predict and manage HE susceptibility in aluminum alloys.

Research typically focuses on one type of aluminum alloy, and comprehensive studies covering multiple types are rare. Additionally, minor changes in alloy composition can lead to different microstructures, potentially affecting hydrogen behavior in the material [109,135,136,140]. Consequently, even studies within the same series of alloys may yield disparate results due to variations in microstructure.

Aluminum alloys may contain hydrogen absorbed during manufacturing, processing, or storage due to exposure to wet environments. This initial hydrogen content should be minimized before testing, as it can impact the results of various measurements, such as hydrogen permeation tests and hydrogen content analysis after pre-charging. However, it is worth noting that many researchers tend to overlook the presence of this initial hydrogen content in aluminum alloys in their studies.

To advance the understanding of HE in aluminum alloys, it is crucial to standardize hydrogen charging methods and measurement techniques. Currently, the lack of standardized methodologies has resulted in significant discrepancies in the results reported by different authors. Such standardization would allow for more reliable comparisons and contribute to the development of alloys with improved resistance to HE.

4.3. Precipitates and Their Influence on HE Susceptibility

Secondary phase particles can affect HE in aluminum alloys through two main mechanisms: by acting as hydrogen traps and accumulating hydrogen in their vicinity and by participating in the hydrogen formation process as part of corrosion, particularly if there is a significant potential difference between the precipitate and the matrix.

The characteristics of precipitates, including their size, shape, and interface with the matrix, and consequently their hydrogen trapping ability, depend on the aging conditions.

Table 13 demonstrates a correlation between the state of the alloy and hydrogen-induced ductility loss.

Table 13. Ductility loss after hydrogenation [%]. Adapted from Refs. [62,102,138–140,162].

	2xxx	6xxx	7xxx	Al–Li
Under-aged, UA	26	x	48	25
Peak-aged, PA	11	0–17	30	17
Over-aged, OA	22	x	16	23

The 6xxx series alloys are considered to have good resistance to HE in peak-aged conditions [27,138]. Consequently, research into other heat treatment states is limited and would benefit from further investigation. After hydrogen saturation, the other alloys showed the greatest decrease in mechanical properties in the under-aged state compared to states with longer aging times. At this stage, the microstructure is dominated by the presence of coherent GP and GPB zones.

The under-aged state alloys have shown the greatest susceptibility to HE. The principle by which precipitates interact with hydrogen at this stage varies significantly depending on the material composition. In the 6xxx and 7xxx series, these precipitates repel hydrogen, while in the 2xxx series, they act as hydrogen traps. This behavior is mainly due to different types of stresses around the GP zones, according to the Gorsky effect. In the 7xxx and 6xxx series, the GP zones have a compressive stress field in contact with the matrix, whereas in the 2xxx series, the GP zones have a tensile stress field, causing hydrogen to transition from a compressive to a tensile stress field [62,79,80].

The low resistance of aluminum alloys in the under-aged state can be attributed to the fact that some types of GP zones do not act as hydrogen traps at all and do not inhibit the diffusion of hydrogen to critical areas in the material [59]. Although the GP zones of the 2xxx series are capable of trapping hydrogen, the desorption curves indicate that the formation of coarser precipitates in the 2xxx series results in stronger binding of hydrogen. GP and GPB zones represent the smallest form of precipitates and, as a consequence, are unlikely to trap hydrogen as effectively as $AlCu_2$ or S phase particles. Additionally, the susceptibility of the 2xxx series at this stage of heat treatment can be attributed to the GBP zones at grain boundaries, where hydrogen accumulates, leading to weakened grain boundaries [25].

In the later stages of heat treatment, the mechanism of hydrogen trapping by different types of precipitates varies significantly between alloy types studied, making it difficult to identify patterns and general dependencies. However, after a longer aging period, hydrogen trapping by the already enlarged secondary phase particles is much more efficient. Although the mechanism of hydrogen trapping varies considerably depending on the composition of the precipitate and its interface with the surrounding matrix, there is generally an improvement in resistance to HE compared to the under-aged state. This is because the precipitates formed in the later stages of heat treatment slow the diffusion of hydrogen by trapping it irreversibly [57–59]. However, if an excessive amount of hydrogen trapping precipitates are present in the material, they may increase susceptibility to HE due to hydrogen-induced decohesion of those particles [9]. An overview of the general effect of precipitates in different stages of heat treatment on HE susceptibility is shown in Figure 17.

Not only do precipitates participate in hydrogen susceptibility of aluminum alloys, but dislocations can intersect coherent precipitates, leading to local softening and formation of concentrated slip planes. These dislocations themselves act as hydrogen traps and facilitate hydrogen transport. Grain boundaries also act as hydrogen traps and can contribute to the embrittlement process [80]. Furthermore, it is challenging to isolate the influence of precipitates from other microstructural constituents. Variations in heat treatment parameters can alter dislocation density and grain boundary characteristics, complicating the study of hydrogen–precipitate interactions. This complexity makes research on the interplay between hydrogen and microstructural features particularly challenging.

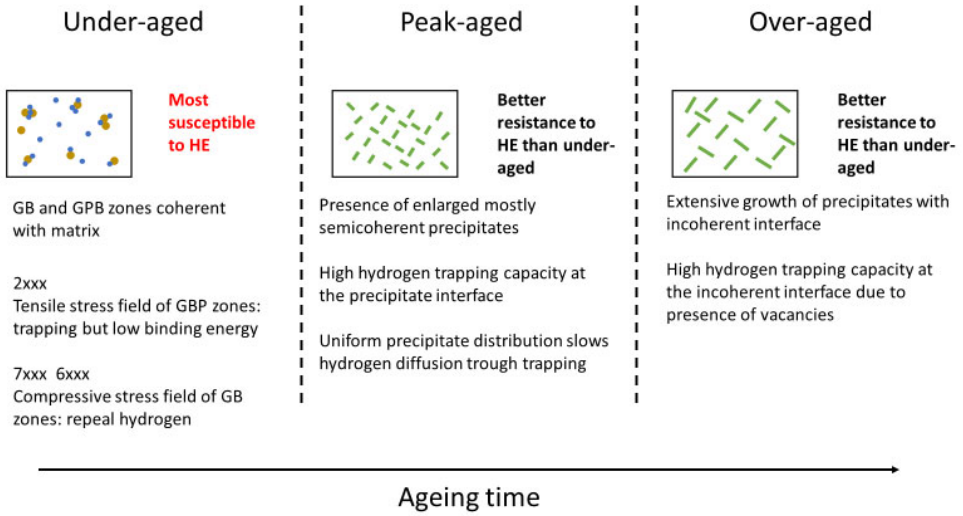

Figure 17. A general summary of the behavior of precipitates towards hydrogen during their evolution.

The concept of mitigating HE in aluminum alloys via precipitates is based on the principle of irreversible hydrogen trapping. A uniform distribution of these particles essentially improves HE resistance in general. However, with a constant source of hydrogen, deep hydrogen traps can become saturated. Once these deep traps are filled, hydrogen that accumulates in reversible trapping sites can contribute to the HE process. Therefore, a thorough quantification of hydrogen trapping and its effects is essential.

Understanding the role of precipitates in HE is critical for improving the performance of aluminum alloys. A key strategy for mitigating HE involves controlling precipitates to optimize mechanical performance while ensuring effective hydrogen trapping. Analyzing the hydrogen trapping ability in different types of aluminum alloys at various stages of aging, and thus with different precipitate characteristics, using standardized approaches, could yield valuable insights. Such research will complement existing knowledge on the interaction of hydrogen with precipitates and could lead to improved methods for precipitate control, ultimately enhancing the resistance of aluminum alloys to HE.

5. Conclusions

- Role of precipitates. Precipitates in aluminum alloys act as hydrogen traps, influencing material susceptibility to HE. The type of interface between precipitates and bulk material (coherent, semi-coherent, or incoherent) plays a critical role in hydrogen trapping.
- Impact of aging.
    - Alloys in the under-aged state, dominated by coherent GP and GPB zones, exhibit the highest susceptibility to HE due to less effective hydrogen trapping.
    - The presence of semi-coherent precipitates in peak-aged alloys leads to moderate susceptibility to HE. Stress fields around precipitates reduce hydrogen diffusion.
    - Incoherent precipitates dominate in the over-aged state. Because these precipitates trap hydrogen strongly, the overall susceptibility to HE decreases compared to the under-aged stage.
- Microstructural evolution. As an alloy undergoes heat treatment, the evolution of secondary phase particles alters how hydrogen interacts with the matrix. Coherency strain and the presence of dislocations at precipitate interfaces are key factors.
- Hydrogen detection. Techniques such as TEMA, APT, and TDA have enhanced the understanding of hydrogen trapping and distribution in aluminum alloys, but further development is needed to accurately study hydrogen–microstructure interactions.
- Future directions. Standardizing hydrogen charging and detection methods is essential to improve the consistency of research outcomes. Understanding the exact

hydrogen trapping mechanism and refining heat treatment processes could lead to the development of alloys with greater resistance to HE.

Author Contributions: Conceptualization, T.K.A., D.R. and P.N.; Writing—Original Draft Preparation, T.K.A. and D.R.; Writing—Review and Editing, T.P. and P.N.; Supervision, T.P.; Funding Acquisition, D.R. and T.P. All authors have read and agreed to the published version of the manuscript.

Funding: This work was supported by the Czech Science Foundation under grant No. 23-06169S and from the grant of specific university research—grant No. A2_FCHT_2024_061.

Data Availability Statement: The data presented in this study are available on request from the corresponding author due to privacy restrictions.

Conflicts of Interest: The authors declare no conflicts of interest.

References

1. Habashi, F. *Extractive Metallurgy of Aluminum. Encyclopedia of Aluminum and Its Alloys, Two-Volume Set (Print)*; CRC Press: Boca Raton, FL, USA, 2018; pp. 893–918.
2. Chi, Y.; Gu, G.; Yu, H.; Chen, C. Laser surface alloying on aluminum and its alloys: A review. *Opt. Laser. Eng.* **2018**, *100*, 23–37. [CrossRef]
3. Kumar, S.; Namboodhiri, T. Precipitation hardening and hydrogen embrittlement of aluminum alloy AA7020. *Bull. Mater. Sci.* **2011**, *34*, 311–321. [CrossRef]
4. Jodeiri, A.; Ashjari, M. 7xxx aluminum alloys; strengthening mechanisms and heat treatment: A review. *Mater. Sci. Eng. Int. J.* **2018**, *2*, 49–53. [CrossRef]
5. Smallman, R.E. *Modern Physical Metallurgy*; Elsevier: Amsterdam, The Netherlands, 2016.
6. Lavernia, E.; Rai, G.; Grant, N. Rapid solidification processing of 7xxx aluminium alloys: A review. *Mater. Sci. Eng.* **1986**, *79*, 211–221. [CrossRef]
7. Bhuiyan, M.S.; Tada, Y.; Toda, H.; Hang, S.; Uesugi, K.; Takeuchi, A.; Sakaguchi, N.; Watanabe, Y. Influences of hydrogen on deformation and fracture behaviors of high Zn 7XXX aluminum alloys. *Int. J. Fract.* **2016**, *200*, 13–29. [CrossRef]
8. Dwivedi, S.K.; Vishwakarma, M. Hydrogen embrittlement in different materials: A review. *Int. J. Hydrogen Energy* **2018**, *43*, 21603–21616. [CrossRef]
9. Safyari, M.; Moshtaghi, M.; Kuramoto, S. On the role of traps in the microstructural control of environmental hydrogen embrittlement of a 7xxx series aluminum alloy. *J. Alloys Compd.* **2021**, *855*, 157300. [CrossRef]
10. Scully, J.R.; Young, G.A.; Smith, S.W. 19—Hydrogen embrittlement of aluminum and aluminum-based alloys. In *Gaseous Hydrogen Embrittlement of Materials in Energy Technologies*; Gangloff, R.P., Somerday, B.P., Eds.; Woodhead Publishing: Sawston, UK, 2012; Volume 2, pp. 707–768.
11. Lynch, S. Hydrogen embrittlement phenomena and mechanisms. *Corros. Rev.* **2012**, *30*, 105–123. [CrossRef]
12. Chen, Y.; Zhao, S.; Ma, H.; Wang, H.; Hua, L.; Fu, S. Analysis of Hydrogen Embrittlement on Aluminum Alloys for Vehicle-Mounted Hydrogen Storage Tanks: A Review. *Metals* **2021**, *11*, 1303. [CrossRef]
13. Symons, D.M. A comparison of internal hydrogen embrittlement and hydrogen environment embrittlement of X-750. *Eng. Fract. Mech.* **2001**, *68*, 751–771. [CrossRef]
14. Tabereaux, A.T.; Peterson, R.D. Chapter 2.5—Aluminum Production. In *Treatise on Process Metallurgy*; Seetharaman, S., Ed.; Elsevier: Boston, MA, USA, 2014; pp. 839–917.
15. Ratvik, A.P.; Mollaabbasi, R.; Alamdari, H. Aluminium production process: From Hall–Héroult to modern smelters. *ChemTexts* **2022**, *8*, 10. [CrossRef]
16. Blackburn, P.E.; Gulbransen, E.A. Aluminum Reactions with Water Vapor, Dry Oxygen, Moist Oxygen, and Moist Hydrogen between 500° and 625 °C. *J. Electrochem. Soc.* **1960**, *107*, 944. [CrossRef]
17. Vojtěch, D. *Kovové Materiály*; Vydavatelství VŠCHT: Prague, Czech Republic, 2006.
18. Cheng, W.-Y.; Wu, S.-D.; Ma, H.-K. Study of tensile strength of aluminum alloy bottle with carbon fiber winding. *Int. J. Hydrogen Energy* **2015**, *40*, 12436–12446. [CrossRef]
19. Gong, L.; Li, Z.; Jin, K.; Gao, Y.; Duan, Q.; Zhang, Y.; Sun, J. Numerical study on the mechanism of spontaneous ignition of high-pressure hydrogen during its sudden release into a tube. *Saf. Sci.* **2020**, *129*, 104807. [CrossRef]
20. Yamabe, J.; Awane, T.; Murakami, Y. Hydrogen trapped at intermetallic particles in aluminum alloy 6061-T6 exposed to high-pressure hydrogen gas and the reason for high resistance against hydrogen embrittlement. *Int. J. Hydrogen Energy* **2017**, *42*, 24560–24568. [CrossRef]
21. Liu, Q.; Atrens, A. A critical review of the influence of hydrogen on the mechanical properties of medium-strength steels. *Corros. Rev.* **2013**, *31*, 85–103. [CrossRef]
22. Li, X.; Ma, X.; Zhang, J.; Akiyama, E.; Wang, Y.; Song, X. Review of Hydrogen Embrittlement in Metals: Hydrogen Diffusion, Hydrogen Characterization, Hydrogen Embrittlement Mechanism and Prevention. *Acta Metall. Sin.–Engl.* **2020**, *33*, 759–773. [CrossRef]

23. Murakami, Y.; Kanezaki, T.; Mine, Y. Hydrogen Effect against Hydrogen Embrittlement. *Mettall. Mater. Trans. A* **2010**, *41*, 2548–2562. [CrossRef]
24. Takasaki, A. High-pressure hydrogen charging of TiAl-based titanium aluminides. *Scr. Mater.* **1998**, *38*, 687–692. [CrossRef]
25. Safyari, M.; Moshtaghi, M.; Kuramoto, S. Environmental hydrogen embrittlement associated with decohesion and void formation at soluble coarse particles in a cold-rolled Al–Cu based alloy. *Mater. Sci. Eng. A* **2021**, *799*, 139850. [CrossRef]
26. Kuramoto, S.; Okahana, J.; Kanno, M. Hydrogen Assisted Intergranular Crack Propagation during Environmental Embrittlement in an Al-Zn-Mg-Cu Alloy. *Mater. Trans.* **2001**, *42*, 2140–2143. [CrossRef]
27. Itoh, G.; Watanabe, M.; Kuroyanagi, K.; Zhao, P.Z. Resistance to hydrogen embrittlement and behavior of hydrogen in 6000 series aluminum alloys. *Mater. Sci. Forum* **2010**, *654–656*, 2899–2902. [CrossRef]
28. Kamoutsi, H.; Haidemenopoulos, G.N.; Bontozoglou, V.; Pantelakis, S. Corrosion-induced hydrogen embrittlement in aluminum alloy 2024. *Corros. Sci.* **2006**, *48*, 1209–1224. [CrossRef]
29. Cottis, R.A. 2.10—Hydrogen Embrittlement. In *Shreir's Corrosion*; Cottis, B., Graham, M., Lindsay, R., Lyon, S., Richardson, T., Scantlebury, D., Stott, H., Eds.; Elsevier: Oxford, UK, 2010; pp. 902–922.
30. Hughes, A.; Muster, T.H.; Boag, A.; Glenn, A.M.; Luo, C.; Zhou, X.; Thompson, G.E.; McCulloch, D. Co-operative corrosion phenomena. *Corros. Sci.* **2010**, *52*, 665–668. [CrossRef]
31. Guillaumin, V.; Mankowski, G. Localized corrosion of 2024 T351 aluminium alloy in chloride media. *Corros. Sci.* **1998**, *41*, 421–438. [CrossRef]
32. Zhao, H.; Chakraborty, P.; Ponge, D.; Hickel, T.; Sun, B.; Wu, C.H.; Gault, B.; Raabe, D. Hydrogen trapping and embrittlement in high-strength Al alloys. *Nature* **2022**, *602*, 437–441. [CrossRef]
33. Petroyiannis, P.V.; Kermanidis, A.T.; Papanikos, P.; Pantelakis, S.G. Corrosion-induced hydrogen embrittlement of 2024 and 6013 aluminum alloys. *Theor. Appl. Fract. Mec.* **2004**, *41*, 173–183. [CrossRef]
34. Wan, D.; Deng, Y.; Barnoush, A. Hydrogen embrittlement effect observed by in-situ hydrogen plasma charging on a ferritic alloy. *Scr. Mater.* **2018**, *151*, 24–27. [CrossRef]
35. Suzuki, H.; Kobayashi, D.; Hanada, N.; Takai, K.; Hagihara, Y. Existing State of Hydrogen in Electrochemically Charged Commercial-Purity Aluminum and Its Effects on Tensile Properties. *Mater. Trans.* **2011**, *52*, 1741–1747. [CrossRef]
36. Kimura, A.; Birnbaum, H.K. Plastic softening by hydrogen plasma charging in pure iron. *Scr. Metall. Mater.* **1987**, *21*, 53–57. [CrossRef]
37. Depover, T.; Hajilou, T.; Wan, D.; Wang, D.; Barnoush, A.; Verbeken, K. Assessment of the potential of hydrogen plasma charging as compared to conventional electrochemical hydrogen charging on dual phase steel. *Mater. Sci. Eng. A* **2019**, *754*, 613–621. [CrossRef]
38. Rozenak, P. Defects producing formation of micro-cracks in aluminum during electrochemical charging with hydrogen. *J. Alloys Compd.* **2005**, *400*, 106–111. [CrossRef]
39. Birnbaum, H.K.; Buckley, C.; Zeides, F.; Sirois, E.; Rozenak, P.; Spooner, S.; Lin, J.S. Hydrogen in aluminum. *J. Alloys Compd.* **1997**, *253–254*, 260–264. [CrossRef]
40. Georgiou, E.P.; Cevallos, V.P.; Van der Donck, T.; Drees, D.; Meersschaut, J.; Panagopoulos, C.N.; Celis, J.P. Effect of cathodic hydrogen charging on the wear behavior of 5754 Al alloy. *Wear* **2017**, *390–391*, 295–301. [CrossRef]
41. Qi, W.J.; Song, R.G.; Qi, X.; Li, H.; Wang, Z.X.; Wang, C.; Jin, J.R. Hydrogen Embrittlement Susceptibility and Hydrogen-Induced Additive Stress of 7050 Aluminum Alloy Under Various Aging States. *J. Mater. Eng. Perform.* **2015**, *24*, 3343–3355. [CrossRef]
42. Dey, S.; Sivaprasad, S.; Das, N.; Chattoraj, I. Influence of Hydrogen on Fatigue Crack Growth in 7075 Aluminum Alloy. *J. Mater. Eng. Perform.* **2023**, *32*, 782–792. [CrossRef]
43. Dey, S.; Chattoraj, I. Interaction of strain rate and hydrogen input on the embrittlement of 7075 T6 Aluminum alloy. *Mat. Sci. Eng. A* **2016**, *661*, 168–178. [CrossRef]
44. Yang, X.; Luo, X.; Zhang, X.; Chen, J.; Gao, L. Characterization of hydrogen in a high strength aluminum alloy. *Mater. Test.* **2020**, *62*, 962–964. [CrossRef]
45. Shen, L.; Chen, H.; Che, X.; Xu, L. Hydrogen embrittlement of the 7B05-T5 aluminum alloy for high-speed trains. *Mater. Corros.* **2020**, *71*, 70–76. [CrossRef]
46. de Bonfils-Lahovary, M.-L.; Josse, C.; Laffont, L.; Blanc, C. Influence of hydrogen on the propagation of intergranular corrosion defects in 2024 aluminium alloy. *Corros. Sci.* **2019**, *148*, 198–205. [CrossRef]
47. Lafouresse, M.C.; de Bonfils-Lahovary, M.-L.; Charvillat, C.; Oger, L.; Laffont, L.; Blanc, C. A Kelvin probe force microscopy study of hydrogen insertion and desorption into 2024 aluminum alloy. *J. Alloys Compd.* **2017**, *722*, 760–766. [CrossRef]
48. Krishnan, M.A.; Raja, V.S. Role of temper conditions on the hydrogen embrittlement behavior of AA 7010. *Corros. Sci.* **2019**, *152*, 211–217. [CrossRef]
49. Smith, S.W.; Scully, J.R. The identification of hydrogen trapping states in an Al-Li-Cu-Zr alloy using thermal desorption spectroscopy. *Mettall. Mater. Trans. A* **2000**, *31*, 179–193. [CrossRef]
50. Saitoh, H.; Iijima, Y.; Tanaka, H. Hydrogen diffusivity in aluminium measured by a glow discharge permeation method. *Acta Metall. Mater.* **1994**, *42*, 2493–2498. [CrossRef]
51. Young, G.A.; Scully, J.R. The diffusion and trapping of hydrogen in high purity aluminum. *Acta Mater.* **1998**, *46*, 6337–6349. [CrossRef]

52. Scully, J.; Young, G.; Smith, S. Hydrogen Solubility, Diffusion and Trapping in High Purity Aluminum and Selected Al-Base Alloys. *Mater. Sci. Forum* **2000**, *331–337*, 1583–1600. [CrossRef]
53. Zakroczymski, T. Adaptation of the electrochemical permeation technique for studying entry, transport and trapping of hydrogen in metals. *Electrochim. Acta* **2006**, *51*, 2261–2266. [CrossRef]
54. Bond, G.M.; Robertson, I.M.; Birnbaum, H.K. Effects of hydrogen on deformation and fracture processes in high-ourity aluminium. *Acta Metall.* **1988**, *36*, 2193–2197. [CrossRef]
55. Hebert, K.R. Trapping of Hydrogen Absorbed in Aluminum during Corrosion. *Electrochim. Acta* **2015**, *168*, 199–205. [CrossRef]
56. Nagumo, M. Hydrogen related failure of steels—A new aspect. *Mater. Sci. Technol.* **2004**, *20*, 940–950. [CrossRef]
57. Turnbull, A.; Hutchings, R.B.; Ferriss, D.H. Modelling of thermal desorption of hydrogen from metals. *Mat. Sci. Eng. A* **1997**, *238*, 317–328. [CrossRef]
58. Pressouyre, G.M. Hydrogen traps, repellers, and obstacles in steel; Consequences on hydrogen diffusion, solubility, and embrittlement. *Metall. Trans. A* **1983**, *14*, 2189–2193. [CrossRef]
59. Oger, L.; Andrieu, E.; Odemer, G.; Peguet, L.; Blanc, C. About the role of the hydrogen during stress corrosion cracking of a low-copper Al-Zn-Mg alloy. *J. Alloys Compd.* **2022**, *900*, 163391. [CrossRef]
60. Adhikari, S.; Chumbley, L.S.; Chen, H.; Jean, Y.C.; Geiculescu, A.C.; Hillier, A.C.; Hebert, K.R. Interfacial voids in aluminum created by aqueous dissolution. *Electrochim. Acta* **2010**, *55*, 6093–6100. [CrossRef]
61. Kozeschnik, E.; Sonderegger, B.; Holzer, I.; Rajek, J.; Cerjak, H. Computer Simulation of the Precipitate Evolution during Industrial Heat Treatment of Complex Alloys. *Mater. Sci. Forum* **2007**, *539–543*, 2431–2436. [CrossRef]
62. Alexopoulos, N.D.; Velonaki, Z.; Stergiou, C.I.; Kourkoulis, S.K. The effect of artificial ageing heat treatments on the corrosion-induced hydrogen embrittlement of 2024 (Al–Cu) aluminium alloy. *Corros. Sci.* **2016**, *102*, 413–424. [CrossRef]
63. Wang, Y.; Sharma, B.; Xu, Y.; Shimizu, K.; Fujihara, H.; Hirayama, K.; Takeuchi, A.; Uesugi, M.; Cheng, G.; Toda, H. Switching nanoprecipitates to resist hydrogen embrittlement in high-strength aluminum alloys. *Nat. Commun.* **2022**, *13*, 6860. [CrossRef]
64. Safyari, M.; Khossossi, N.; Meisel, T.; Dey, P.; Prohaska, T.; Moshtaghi, M. New insights into hydrogen trapping and embrittlement in high strength aluminum alloys. *Corros. Sci.* **2023**, *223*, 111453. [CrossRef]
65. Safyari, M.; Moshtaghi, M.; Hojo, T.; Akiyama, E. Mechanisms of hydrogen embrittlement in high-strength aluminum alloys containing coherent or incoherent dispersoids. *Corros. Sci.* **2022**, *194*, 109895. [CrossRef]
66. Birnbaum, H.K.; Sofronis, P. Hydrogen-enhanced localized plasticity—A mechanism for hydrogen-related fracture. *Mat. Sci. Eng. A* **1994**, *176*, 191–202. [CrossRef]
67. Lynch, S.P. Metallographic contributions to understanding mechanisms of environmentally assisted cracking. *Metallography* **1989**, *23*, 147–171. [CrossRef]
68. Tarzimoghadam, Z.; Rohwerder, M.; Merzlikin, S.V.; Bashir, A.; Yedra, L.; Eswara, S.; Ponge, D.; Raabe, D. Multi-scale and spatially resolved hydrogen mapping in a Ni–Nb model alloy reveals the role of the δ phase in hydrogen embrittlement of alloy 718. *Acta Mater.* **2016**, *109*, 69–81. [CrossRef]
69. Lynch, S. Metallographic and fractographic techniques for characterising and understanding hydrogen-assisted cracking of metals. In *Gaseous Hydrogen Embrittlement of Materials in Energy Technologies*; Elsevier: Amsterdam, The Netherlands, 2012; pp. 274–346.
70. Martin, M.L.; Dadfarnia, M.; Nagao, A.; Wang, S.; Sofronis, P. Enumeration of the hydrogen-enhanced localized plasticity mechanism for hydrogen embrittlement in structural materials. *Acta Mater.* **2019**, *165*, 734–750. [CrossRef]
71. Lynch, S. Discussion of some recent literature on hydrogen-embrittlement mechanisms: Addressing common misunderstandings. *Corros. Rev.* **2019**, *37*, 377–395. [CrossRef]
72. Magee, C.W.; Botnick, E.M. Hydrogen depth profiling using SIMS—Problems and their solutions. *J. Vac. Sci. Technol.* **1981**, *19*, 47–52. [CrossRef]
73. Koyama, M.; Rohwerder, M.; Tasan, C.C.; Bashir, A.; Akiyama, E.; Takai, K.; Raabe, D.; Tsuzaki, K. Recent progress in microstructural hydrogen mapping in steels: Quantification, kinetic analysis, and multi-scale characterisation. *Mater. Sci. Technol.* **2017**, *33*, 1481–1496. [CrossRef]
74. Bond, G.M.; Robertson, I.M.; Birnbaum, H.K. The influence of hydrogen on deformation and fracture processes in high-strength aluminum alloys. *Acta Metall.* **1987**, *35*, 2289–2296. [CrossRef]
75. Rozenak, P.; Sirois, E.; Ladna, B.; Birnbaum, H.K.; Spooner, S. Characterization of hydrogen defects forming during chemical charging in the aluminum. *J. Alloys Compd.* **2005**, *387*, 201–210. [CrossRef]
76. Larignon, C.; Alexis, J.; Andrieu, E.; Lacroix, L.; Odemer, G.; Blanc, C. Investigation of Kelvin probe force microscopy efficiency for the detection of hydrogen ingress by cathodic charging in an aluminium alloy. *Scr. Mater.* **2013**, *68*, 479–482. [CrossRef]
77. Larignon, C.; Alexis, J.; Andrieu, E.; Lacroix, L.; Odemer, G.; Blanc, C. Combined Kelvin probe force microscopy and secondary ion mass spectrometry for hydrogen detection in corroded 2024 aluminium alloy. *Electrochim. Acta* **2013**, *110*, 484–490. [CrossRef]
78. Iijima, Y.; Yoshida, S.; Saitoh, H. Hydrogen trapping in an Al-2.1 wt % Li alloy. *J. Mater. Sci.* **1995**, *30*, 1290–1294. [CrossRef]
79. Iijima, Y.; Yoshida, S.-I.; Saitoh, H.; Tanaka, H.; Hirano, K.-I. Hydrogen trapping and repelling in an Al-6 wt% Zn-2 wt% Mg alloy. *J. Mater. Sci.* **1992**, *27*, 5735–5738. [CrossRef]
80. Saitoh, H.; Iijima, Y.; Hirano, K. Behaviour of hydrogen in pure aluminium, Al-4 mass% Cu and Al-1 mass% Mg2Si alloys studied by tritium electron microautoradiography. *J. Mater. Sci.* **1994**, *29*, 5739–5744. [CrossRef]

81. Saitoh, H.; Iijima, Y. Intensity of hydrogen trapping in pure Al, Al-4 wt% Cu and Al-1 wt% Mg_2Si alloys measured by tritium release. *J. Mater. Sci. Lett.* **1994**, *13*, 1092–1094. [CrossRef]
82. Chen, Y.-S.; Liu, P.-Y.; Niu, R.; Devaraj, A.; Yen, H.-W.; Marceau, R.K.W.; Cairney, J.M. Atom Probe Tomography for the Observation of Hydrogen in Materials: A Review. *Microsc. Microanal.* **2022**, *29*, 1–15. [CrossRef]
83. He, Q.; Jiang, J.; Wang, X.; Chen, J.; Shao, W.; Zhen, L. Insight into Intergranular Corrosion of the Aluminum Alloy 2024-T3: Effect of Pre-Charged Hydrogen. *J. Electrochem. Soc.* **2023**, *170*, 041501. [CrossRef]
84. Gong, S.-H.; Lee, J.-Y.; Kim, Y.-J. Atom-Probe Tomographic and Electron Microscopic Analyses of a High Strength 7075-T4 Aluminum Alloy. *J. Nanosci. Nanotechno.* **2019**, *19*, 4182–4187. [CrossRef]
85. Parvizi, R.; Marceau, R.K.W.; Hughes, A.E.; Tan, M.Y.; Forsyth, M. Atom Probe Tomography Study of the Nanoscale Heterostructure around an $Al_{20}Mn_3Cu_2$ Dispersoid in Aluminum Alloy 2024. *Langmuir* **2014**, *30*, 14817–14823. [CrossRef]
86. Sun, X.Y.; Zhang, B.; Lin, H.Q.; Zhou, Y.; Sun, L.; Wang, J.Q.; Han, E.H.; Ke, W. Atom probe tomographic study of elemental segregation at grain boundaries for a peak-aged Al–Zn–Mg alloy. *Corros. Sci.* **2014**, *79*, 1–4. [CrossRef]
87. Safyari, M.; Rauscher, A.; Ucsnik, S.; Moshtaghi, M. Hydrogen trapping and permeability in carbon fiber reinforced aluminum alloys. *Int. J. Hydrogen Energy* **2024**, *50*, 199–210. [CrossRef]
88. Oger, L.; Lafouresse, M.C.; Odemer, G.; Peguet, L.; Blanc, C. Hydrogen diffusion and trapping in a low copper 7xxx aluminium alloy investigated by Scanning Kelvin Probe Force Microscopy. *Mat. Sci. Eng. A* **2017**, *706*, 126–135. [CrossRef]
89. Oger, L.; Malard, B.; Odemer, G.; Peguet, L.; Blanc, C. Influence of dislocations on hydrogen diffusion and trapping in an Al-Zn-Mg aluminium alloy. *Mater. Des.* **2019**, *180*, 107901. [CrossRef]
90. Salmi, S.; Rhode, M.; Jüttner, S.; Zinke, M. Hydrogen determination in 22MnB5 steel grade by use of carrier gas hot extraction technique. *Weld. World* **2015**, *59*, 137–144. [CrossRef]
91. Kamoutsi, H.; Haidemenopoulos, G.N.; Mavros, H.; Karantonidis, C.; Floratos, P.; Alhosani, Z.; Cho, P.; Anjum, D.H.; Ravaux, F.; Polychronopoulou, K. Effect of precipitate coherency on the corrosion-induced hydrogen trapping in 2024 aluminum alloy. *Int. J. Hydrogen Energy* **2021**, *46*, 34487–34497. [CrossRef]
92. Charitidou, E.; Papapolymerou, G.; Haidemenopoulos, G.N.; Hasiotis, N.; Bontozoglou, V. Characterization of trapped hydrogen in exfoliation corroded aluminium alloy 2024. *Scr. Mater.* **1999**, *41*, 1327–1332. [CrossRef]
93. Kamoutsi, H.; Haidemenopoulos, G.N.; Bontozoglou, V.; Petroyiannis, P.V.; Pantelakis, S.G. Effect of prior deformation and heat treatment on the corrosion-induced hydrogen trapping in aluminium alloy 2024. *Corros. Sci.* **2014**, *80*, 139–142. [CrossRef]
94. Safyari, M.; Moshtaghi, M.; Kuramoto, S.; Hojo, T. Influence of microstructure-driven hydrogen distribution on environmental hydrogen embrittlement of an Al–Cu–Mg alloy. *Int. J. Hydrogen Energy* **2021**, *46*, 37502–37508. [CrossRef]
95. Moshtaghi, M.; Safyari, M.; Kuramoto, S.; Hojo, T. Unraveling the effect of dislocations and deformation-induced boundaries on environmental hydrogen embrittlement behavior of a cold-rolled Al–Zn–Mg–Cu alloy. *Int. J. Hydrogen Energy* **2021**, *46*, 8285–8299. [CrossRef]
96. Wei, F.-G.; Enomoto, M.; Tsuzaki, K. Applicability of the Kissinger's formula and comparison with the McNabb–Foster model in simulation of thermal desorption spectrum. *Comp. Mater. Sci.* **2012**, *51*, 322–330. [CrossRef]
97. Danielson, M.J. Use of the Devanathan–Stachurski cell to measure hydrogen permeation in aluminum alloys. *Corros. Sci.* **2002**, *44*, 829–840. [CrossRef]
98. Zheng, C.-b.; Yan, B.-h.; Zhang, K.; Yi, G. Electrochemical investigation on the hydrogen permeation behavior of 7075-T6 Al alloy and its influence on stress corrosion cracking. *Int. J. Min. Met. Mater.* **2015**, *22*, 729–737. [CrossRef]
99. Ai, J.-H.; Lim, M.L.C.; Scully, J.R. Effective Hydrogen Diffusion in Aluminum Alloy 5083-H131 as a Function of Orientation and Degree of Sensitization. *Corrosion* **2013**, *69*, 1225–1239. [CrossRef] [PubMed]
100. Qi, W.J.; Song, R.G.; Zhang, Y.; Wang, C.; Qi, X.; Li, H. Study on mechanical properties and hydrogen embrittlement susceptibility of 7075 aluminium alloy. *Corros. Eng. Sci. Technol.* **2015**, *50*, 480–486. [CrossRef]
101. Chen, L.; Chen, W.; Liu, Z.; Shao, Y.; Hu, Z. Effects of hydrogen on mechanical properties and fracture mechanism of 8090 Al-Li alloy. *Metall. Trans. A* **1993**, *24*, 1355–1361. [CrossRef]
102. Albrecht, J.; Thompson, A.W.; Bernstein, I.M. The role of microstructure in hydrogen-assisted fracture of 7075 aluminum. *Metall. Trans. A* **1979**, *10*, 1759–1766. [CrossRef]
103. Prasad, K.S. Solid State Phase Transformations in AA 8090 Al-Li Alloys. Ph.D. Thesis, University of Roorkee, Roorkee, India, 1999.
104. Sekhar, A.P.; Nandy, S.; Ray, K.K.; Das, D. Prediction of Aging Kinetics and Yield Strength of 6063 Alloy. *J. Mater. Eng. Perform.* **2019**, *28*, 2764–2778. [CrossRef]
105. Moy, C.K.S.; Weiss, M.; Xia, J.; Sha, G.; Ringer, S.P.; Ranzi, G. Influence of heat treatment on the microstructure, texture and formability of 2024 aluminium alloy. *Mat. Sci. Eng. A* **2012**, *552*, 48–60. [CrossRef]
106. Wang, S.C.; Starink, M.J. Two types of S phase precipitates in Al–Cu–Mg alloys. *Acta Mater.* **2007**, *55*, 933–941. [CrossRef]
107. Winkelman, G.B.; Raviprasad, K.; Muddle, B.C. Orientation relationships and lattice matching for the S phase in Al–Cu–Mg alloys. *Acta Mater.* **2007**, *55*, 3213–3228. [CrossRef]
108. Robson, J.D. Microstructural evolution in aluminium alloy 7050 during processing. *Mat. Sci. Eng. A* **2004**, *382*, 112–121. [CrossRef]
109. Buha, J.; Lumley, R.N.; Crosky, A.G.; Hono, K. Secondary precipitation in an Al–Mg–Si–Cu alloy. *Acta Mater.* **2007**, *55*, 3015–3024. [CrossRef]
110. Chauhan, K. Influence of Heat Treatment on the Mechanical Properties of Aluminium Alloys (6xxx Series): A Literature Review. *Int. J. Eng. Res. Technol.* **2017**, *6*, 386–389. [CrossRef]

111. *Heat Treating of Nonferrous Alloys*; ASM International: Almere, The Netherlands, 2016.
112. Wang, L.; Sun, J.; Zhu, X.; Cheng, L.; Shi, Y.; Guo, L.; Yan, B. Effects of T2 Heat Treatment on Microstructure and Properties of the Selective Laser Melted Aluminum Alloy Samples. *Materials* **2018**, *11*, 66. [CrossRef] [PubMed]
113. Liscic, B.; Tensi, H.M.; Canale, L.C.; Totten, G.E. *Quenching Theory and Technology*; CRC Press: Boca Raton, FL, USA, 2010.
114. Özyürek, D.; Tunçay, T.; Kaya, H. The Effects of T5 and T6 Heat Treatments on Wear Behaviour of AA6063 Alloy. *High Temp. Mater. Process.* **2014**, *33*, 231–237. [CrossRef]
115. Rambabu, P.; Eswara Prasad, N.; Kutumbarao, V.V.; Wanhill, R.J.H. Aluminium Alloys for Aerospace Applications. In *Aerospace Materials and Material Technologies: Volume 1: Aerospace Materials*; Prasad, N.E., Wanhill, R.J.H., Eds.; Springer Singapore: Singapore, 2017; pp. 29–52.
116. Lacroix, L.; Ressier, L.; Blanc, C.; Mankowski, G. Combination of AFM, SKPFM, and SIMS to Study the Corrosion Behavior of S-phase particles in AA2024-T351. *J. Electrochem. Soc.* **2008**, *155*, C131. [CrossRef]
117. Bagaryatsky, Y.A. Structural changes on aging Al-Cu-Mg alloys. *Dokl. Akad. SSSR* **1952**, *87*, 397–559.
118. Ringer, S.P.; Sakurai, T.; Polmear, I.J. Origins of hardening in aged Al-Gu-Mg-(Ag) alloys. *Acta Mater.* **1997**, *45*, 3731–3744. [CrossRef]
119. Kovarik, L.; Court, S.A.; Fraser, H.L.; Mills, M.J. GPB zones and composite GPB/GPBII zones in Al–Cu–Mg alloys. *Acta Mater.* **2008**, *56*, 4804–4815. [CrossRef]
120. Shen, Z.; Ding, Q.; Liu, C.; Wang, J.; Tian, H.; Li, J.; Zhang, Z. Atomic-scale mechanism of the $\theta'' \rightarrow \theta'$ phase transformation in Al-Cu alloys. *J. Mater. Sci. Technol.* **2017**, *33*, 1159–1164. [CrossRef]
121. Chen, Z.; Zhao, Y.; Zhang, Z. Theoretical and experimental study of precipitation and coarsening kinetics of θ' phase in Al–Cu alloy. *Vacuum* **2021**, *189*, 110263. [CrossRef]
122. Jones, D.A. *Principles and Prevention of Corrosion*; Prentice Hall: Hoboken, NJ, USA, 1996.
123. Kosari, A.; Zandbergen, H.; Tichelaar, F.; Visser, P.; Taheri, P.; Terryn, H.; Mol, J.M.C. In-situ nanoscopic observations of dealloying-driven local corrosion from surface initiation to in-depth propagation. *Corros. Sci.* **2020**, *177*, 108912. [CrossRef]
124. Scamans, G.M. Embrittlement of Aluminum Alloys Exposed to Water Vapour. *Environ.-Sensitive Fract. Eng. Mater.* **1977**, 464-383.
125. Shao, S.; Akasheh, F.; Wang, J.; Liu, Y. Alternative misfit dislocations pattern in semi-coherent FCC {100} interfaces. *Acta Mater.* **2018**, *144*, 177–186. [CrossRef]
126. Alexopoulos, N.D.; Dietzel, W. Effect of corrosion-induced hydrogen embrittlement and its degradation impact on tensile properties and fracture toughness of (Al-Cu-Mg) 2024 alloy. *Procedia Struct. Integr.* **2016**, *2*, 573–580. [CrossRef]
127. Zeides, F.; Roman, I. Study of hydrogen embrittlement in aluminium alloy 2024 in the longitudinal direction. *Mat. Sci. Eng. A* **1990**, *125*, 21–30. [CrossRef]
128. Kermanidis, A.T.; Stamatelos, D.G.; Labeas, G.N.; Pantelakis, S.G. Tensile behaviour of corroded and hydrogen embrittled 2024 T351 aluminum alloy specimen. *Theor. Appl. Fract. Mec.* **2006**, *45*, 148–158. [CrossRef]
129. Feng, Z.; Luo, X.; Chen, Y.; Chen, N.; Wu, G. Surface severe plastic deformation induced solute and precipitate redistribution in an Al-Cu-Mg alloy. *J. Alloys Compd.* **2019**, *773*, 585–596. [CrossRef]
130. Larignon, C.; Alexis, J.; Andrieu, E.; Odemer, G.; Blanc, C. The contribution of hydrogen to the corrosion of 2024 aluminium alloy exposed to thermal and environmental cycling in chloride media. *Corros. Sci.* **2013**, *69*, 211–220. [CrossRef]
131. Hirth, S.M.; Marshall, G.J.; Court, S.A.; Lloyd, D.J. Effects of Si on the aging behaviour and formability of aluminium alloys based on AA6016. *Mat. Sci. Eng. A* **2001**, *319–321*, 452–456. [CrossRef]
132. Baruah, M.; Borah, A. Processing and precipitation strengthening of 6xxx series aluminium alloys: A review. *Int. J. Mater. Sci* **2020**, *1*, 40–48. [CrossRef]
133. Guo, M.X.; Zhang, X.K.; Zhang, J.S.; Zhuang, L.Z. Effect of Zn addition on the precipitation behaviors of Al–Mg–Si–Cu alloys for automotive applications. *J. Mater. Sci.* **2017**, *52*, 1390–1404. [CrossRef]
134. Matsuda, K.; Sakaguchi, Y.; Miyata, Y.; Uetani, Y.; Sato, T.; Kamio, A.; Ikeno, S. Precipitation sequence of various kinds of metastable phases in Al-1.0mass% Mg2Si-0.4mass% Si alloy. *J. Mater. Sci.* **2000**, *35*, 179–189. [CrossRef]
135. Gaber, A.; Ali, A.M.; Matsuda, K.; Kawabata, T.; Yamazaki, T.; Ikeno, S. Study of the developed precipitates in Al–0.63Mg–0.37Si–0.5Cu(wt.%) alloy by using DSC and TEM techniques. *J. Alloys Compd.* **2007**, *432*, 149–155. [CrossRef]
136. Ichitani, K.; Koyama, K. Effect of experimental humidity on fatigue fracture of 6XXX-series aluminum alloys. In *Furukawa-Sky Review/Furukawa-Sky Review*; Furukawa Sky Co., Ltd.: Tokyo, Japan, 2012; pp. 15–21.
137. Dumolt, S.D.; Laughlin, D.E.; Williams, J.C. Formation of a modified β' phase in aluminum alloy 6061. *Scr. Metall. Mater.* **1984**, *18*, 1347–1350. [CrossRef]
138. Ando, M.; Kanno, M.; Ichitani, K.; Motegi, T. Effects of alloy compositions on hydrogen embrittlement of Al–Mg–Si based alloys. *J. Jpn. Inst. Light Met.* **2009**, *59*, 81–86. [CrossRef]
139. Osaki, S.; Kondo, H.; Kinoshita, K. Contribution of hydrogen embrittlement to SCC process in excess Si type Al-Mg-Si alloys. *Mater. Trans.* **2006**, *47*, 1127–1134. [CrossRef]
140. Horikawa, K.; Matsubara, T.; Kobayashi, H. Hydrogen charging of Al–Mg–Si-based alloys by friction in water and its effect on tensile properties. *Mat. Sci. Eng. A* **2019**, *764*, 138199. [CrossRef]
141. Hachet, G.; Sauvage, X. Influence of hydrogen vacancy interactions on natural and artificial ageing of an AlMgSi alloy. *J. Alloys Compd.* **2022**, *905*, 164251. [CrossRef]

142. Priya, P.; Johnson, D.R.; Krane, M.J.M. Precipitation during cooling of 7XXX aluminum alloys. *Comp. Mater. Sci.* **2017**, *139*, 273–284. [CrossRef]
143. Liao, Y.-g.; Han, X.-q.; Zeng, M.-x.; Jin, M. Influence of Cu on microstructure and tensile properties of 7XXX series aluminum alloy. *Mater. Des.* **2015**, *66*, 581–586. [CrossRef]
144. Christodoulou, L.; Flower, H.M. Hydrogen embrittlement and trapping in Al6%-Zn-3%-Mg. *Acta Metall.* **1980**, *28*, 481–487. [CrossRef]
145. Gest, R.; Troiano, A. Stress corrosion and hydrogen embrittlement in an aluminum alloy. *Corrosion* **1974**, *30*, 274–279. [CrossRef]
146. El-Amoush, A.S. An investigation of hydrogen-induced hardening in 7075-T6 aluminum alloy. *J. Alloys Compd.* **2008**, *465*, 497–501. [CrossRef]
147. Thompson, A.W.; Bernstein, I.M. The Role of Metallurgical Variables in Hydrogen-Assisted Environmental Fracture. In *Advances in Corrosion Science and Technology*; Fontana, M.G., Staehle, R.W., Eds.; Springer US: Boston, MA, USA, 1980; pp. 53–175.
148. Takano, N. Hydrogen diffusion and embrittlement in 7075 aluminum alloy. *Mat. Sci. Eng. A* **2008**, *483–484*, 336–339. [CrossRef]
149. Thompson, A.W. The behavior of sensitized 309S stainless steel in hydrogen. *Mater. Sci. Eng.* **1974**, *14*, 253–264. [CrossRef]
150. Thompson, A.W. Hydrogen embrittlement of stainless steels by lithium hydride. *Metall. Trans.* **1973**, *4*, 2819–2825. [CrossRef]
151. Louthan, M.R.; Caskey, G.R.; Donovan, J.A.; Rawl, D.E. Hydrogen embrittlement of metals. *Mater. Sci. Eng.* **1972**, *10*, 357–368. [CrossRef]
152. Aboura, Y.; Garner, A.J.; Euesden, R.; Barrett, Z.; Engel, C.; Holroyd, N.J.H.; Prangnell, P.B.; Burnett, T.L. Understanding the environmentally assisted cracking (EAC) initiation and propagation of new generation 7xxx alloys using slow strain rate testing. *Corros. Sci.* **2022**, *199*, 110161. [CrossRef]
153. Bal, B.; Okdem, B.; Bayram, F.C.; Aydin, M. A detailed investigation of the effect of hydrogen on the mechanical response and microstructure of Al 7075 alloy under medium strain rate impact loading. *Int. J. Hydrogen Energy* **2020**, *45*, 25509–25522. [CrossRef]
154. Euesden, R.T.; Aboura, Y.; Garner, A.J.; Jailin, T.; Grant, C.; Barrett, Z.; Engel, C.; Shanthraj, P.; Holroyd, N.J.H.; Prangnell, P.B.; et al. In-situ observation of environmentally assisted crack initiation and short crack growth behaviour of new-generation 7xxx series alloys in humid air. *Corros. Sci.* **2023**, *216*, 111051. [CrossRef]
155. Yusheng, C.; Ziyong, Z.; Sue, L.; Wei, K.; Yun, Z.; Wanming, Z. The corrosion behaviors and mechanism of 1420 Al-Li alloy. *Scr. Mater.* **1996**, *34*, 781–786. [CrossRef]
156. Starke, E.A.; Sanders, T.H.; Palmer, I.G. New Approaches to Alloy Development in the Al-Li System. *JOM* **1981**, *33*, 24–33. [CrossRef]
157. Prasad, K.S.; Prasad, N.E.; Gokhale, A.A. Chapter 4—Microstructure and Precipitate Characteristics of Aluminum–Lithium Alloys. In *Aluminum-lithium Alloys*; Eswara Prasad, N., Gokhale, A.A., Wanhill, R.J.H., Eds.; Butterworth-Heinemann: Boston, MA, USA, 2014; pp. 99–137.
158. Gutierrez-Urrutia, I.; Gutierrez-Saiz, S.; Bocanegra, E.H.; Nó, M.; San Juan, J. Analysis of delta Prime precipitation in Al-Li alloys. *Mater. Sci. Forum* **2002**, *396–402*, 881–886. [CrossRef]
159. Bennett, C.G.; Lynch, S.P.; Nethercott, R.B.; Kerr, M.; Sweet, E.D. Fracture toughness of 2090 Al–Li–Cu extrusions with high and low hydrogen contents. *Mat. Sci. Eng. A* **1998**, *247*, 32–39. [CrossRef]
160. Meletis, E.I.; Huang, W. The role of the T1 phase in the pre-exposure and hydrogen embrittlement of AlLiCu alloys. *Mater. Sci. Eng. A* **1991**, *148*, 197–209. [CrossRef]
161. Wang, X.; Li, G.; He, Q.; Xiao, E.; Jiang, J.; Shao, W.; Zhen, L. Hydrogen trapping and embrittlement susceptibility in Al-Cu-Li alloys. *Corros. Sci.* **2024**, *226*, 111628. [CrossRef]
162. Thakur, C.; Balasubramaniam, R. Hydrogen embrittlement of aged and retrogressed-reaged Al-Li-Cu-Mg alloys. *Acta Mater.* **1997**, *45*, 1323–1332. [CrossRef]